MAP7 directs apical cytoskeletal remodeling to establish Sertoli cell polarity and support germ cell development

Koji Kikuchi[1,7,8*], Toshihiko Fujimori[2], Mami Nakagawa[2], Keisuke Ohta[3], Ryuki Shimada[1], Sayoko Fujimura[4], Kei-ichiro Yasunaga[4], Shingo Usuki[4], Naoki Tani[4], Akira Nakamura[5], Kimi Araki[6], and Kei-ichiro Ishiguro[1,7,8]

[1]Department of Chromosome Biology, Institute of Molecular Embryology and Genetics, Kumamoto University, 2-2-1 Honjo, Chuo-ku, Kumamoto 860-0811, Japan

[2]Division of Embryology, National Institute for Basic Biology, 5-1 Higashiyama, Myodaiji, Okazaki, Aichi 444-8787, Japan

[3]Advanced Imaging Research Center, Kurume University School of Medicine, 67 Asahimachi, Kurume, Fukuoka 830-0011, Japan.

[4]Liaison Laboratory Research Promotion Center, Institute of Molecular Embryology and Genetics, Kumamoto University, 2-2-1 Honjo, Chuo-ku, Kumamoto 860-0811, Japan

[5]Department of Germline Development, Institute of Molecular Embryology and Genetics, Kumamoto University, 2-2-1 Honjo, Chuo-ku, Kumamoto 860-0811, Japan

[6]Institute of Resource Development and Analysis, Kumamoto University, 2-2-1 Honjo, Chuo-ku, Kumamoto 860-0811, Japan

Present address:

[7]Division of Comparative Pathophysiology, Next Generation In Vivo Research Exploratory Center (cNIVR), Chiba University, 1-8-1 Inohana, Chuo-ku, Chiba 260-8670, Japan

[8]Department of Biomedical Science, Graduate School of Medicine, Chiba University, 1-8-1 Inohana, Chuo-ku, Chiba 260-8670, Japan

***Corresponding author**: kojik@chiba-u.jp (K.K.)

Classification: Biological Sciences (Cell Biology; Developmental Biology)

Keywords: MAP7, Cytoskeletal remodeling, Epithelial polarity, Apical domain, Meiosis

Abstract

Sertoli cells establish a specialized apical domain that organizes the seminiferous epithelium and supports germ cell development, yet how this domain emerges during early postnatal polarization and becomes functionally linked to germ cell maturation remains unclear. Here, we identify the microtubule-associated protein MAP7 as a key regulator of the cytoskeletal organization required for apical domain formation. MAP7 localizes to apical microtubules that are distinct from stable, acetylated microtubules, and native-tissue imaging shows that these MAP7-decorated microtubules, initially lacking directionality, progressively acquire longitudinal orientation as Sertoli cells polarize. In *Map7*-deficient testes, overall microtubule abundance is maintained, but their spatial organization is severely disrupted, accompanied by persistent luminal F-actin accumulation. These defects impair apical domain maturation and block lumen formation during the first wave of spermatogenesis, coinciding with ectopic expansion of tight junctions. Proteomic analysis identified the non-muscle myosin II heavy chains MYH9 and MYH10 among MAP7-associated proteins in polarizing Sertoli cells. MYH9 normally becomes enriched at luminal regions where microtubules and F-actin converge, but remains diffuse in *Map7*-deficient Sertoli cells despite the persistence of ectopic luminal cytoskeletal structures, suggesting that MAP7 contributes to the cytoskeletal context required for proper NMII positioning. Single-cell RNA sequencing shows that Sertoli cell differentiation largely proceeds without MAP7, whereas germ cells exhibit delayed meiotic progression with expanded pachytene subtypes. Together, these findings establish MAP7-dependent microtubule remodeling as a critical organizing mechanism for apical domain formation and reveal how cytoskeletal architecture within Sertoli cells contributes to the structural environment required for timely germ cell development.

(248 words)

Significance statement

Epithelial polarity is essential for tissue organization, yet how microtubules are dynamically remodeled to form a functional apical domain *in vivo* remains unclear. Sertoli cells offer a unique context in which apical domain formation is tightly linked to germ cell development. Using genetic models, native-tissue imaging, and proteomics, we identify MAP7 as a key organizer of the apical microtubule network during postnatal testis development. Loss of MAP7 disrupts directional microtubule organization, impairs apical domain maturation, alters junctional architecture, and delays meiotic progression of germ cells. These findings reveal a previously uncharacterized role for microtubule organization in coordinating epithelial polarity with germ cell maturation, highlighting cytoskeletal architecture as a structural regulator of tissue-level differentiation.

Introduction

Sertoli cells are highly specialized epithelial cells that form the architectural scaffold of the seminiferous epithelium and orchestrate spermatogenesis. Unlike classical columnar epithelia, they undergo a unique form of polarization during postnatal development, culminating in the establishment of a distinct apical domain. This domain is essential for organizing the three-dimensional structure of the seminiferous tubules and generating a microenvironment that supports germ cell differentiation. As germ cells migrate from the basal to the luminal compartment, the Sertoli cell apical domain provides structural support and facilitates the localized delivery of trophic factors, adhesive interactions, and signaling cues required for maturation (1). Disruption of apical architecture impairs germ cell development and causes male infertility, underscoring the physiological importance of Sertoli cell polarity (2-5). Despite this significance, the developmental progression through which Sertoli cells acquire polarity, and how this process enables formation of a functional apical domain, remain incompletely understood.

Sertoli cell polarity is established and maintained through dynamic cytoskeletal remodeling (6). Actin filaments, key components of ectoplasmic specializations (ES), coordinate cell–cell adhesion and junctional integrity among Sertoli cells and between Sertoli cells and germ cells (7, 8). Basal ES comprises actin-based adherens, tight, and gap junctions that contribute to the blood–testis barrier (BTB), whereas apical ES supports Sertoli–spermatid adhesion and maturation. Deletion of Sertoli-specific small GTPases, such as RAC1 and CDC42, which regulate actin organization, disrupts apical ES formation and Sertoli cell polarity (4, 5). By contrast, the contribution of the microtubule cytoskeleton to Sertoli cell polarization has been less extensively characterized. Microtubules form longitudinal bundles along the apical–basal axis and have been proposed to mediate intracellular transport and structural organization. Perturbations of microtubule architecture—such as Sertoli cell-specific overexpression of γ-tubulin (9, 10) , expression of a dominant-negative EB1 variant (11) , or loss of the microtubule-severing enzyme KATNAL1 (12)—lead to spermatogenic defects, highlighting the importance of microtubule remodeling. However, how microtubules are dynamically reorganized during the establishment of Sertoli cell polarity in the early postnatal testis remains largely uncharacterized.

Microtubule dynamics are regulated by numerous microtubule-associated proteins (MAPs) (13, 14). Among these, the MAP7 family has emerged as a key regulator of microtubule organization in cultured cells and in *Drosophila*. MAP7 proteins contain an N-terminal microtubule-binding domain and a C-terminal kinesin-1–binding domain, enabling

them to influence microtubule stability and motor recruitment (15-23). MAP7 also competes with other MAPs for microtubule association, shaping motor protein distribution in neurons (24, 25). In HeLa cells, MAP7 and MAP7D1 cooperatively guide microtubule plus ends to the cortex during migration and adhesion (18). In mice, MAP7 is expressed in both Sertoli and germ cells (26, 27), and *Map7* gene-trap mutants exhibit reduced microtubule bundling in Sertoli cells and structural abnormalities in spermatid manchettes (27). These findings suggest a role for MAP7 in microtubule organization, but whether MAP7 contributes to the dynamic remodeling events that accompany Sertoli cell polarization remains unresolved.

We address these questions by identifying MAP7 as a pivotal regulator of cytoskeletal organization during the establishment of Sertoli cell polarity and examining how it coordinates microtubule organization, apical domain formation, and germ cell maturation. Our findings reveal that MAP7 associates with a population of apical microtubules that is distinct from stable, acetylated microtubules, and that these MAP7-decorated microtubules progressively acquire longitudinal orientation as polarization advances. Loss of MAP7 preserves overall microtubule abundance but severely disrupts their spatial organization, accompanied by aberrant luminal actin accumulation, impaired apical domain maturation, failure of lumen formation, and abnormal expansion of tight junctions. Proteomic analysis of polarizing Sertoli cells identified the non-muscle myosin II heavy chains MYH9 and MYH10 among MAP7-associated proteins. Interestingly, MYH9, which normally concentrates at luminal regions where microtubules and F-actin converge, was altered in *Map7*-deficient Sertoli cells, highlighting a spatial correspondence between the two cytoskeletal systems during apical domain formation. Finally, single-cell RNA sequencing shows that Sertoli cell differentiation proceeds largely without MAP7, whereas germ cells exhibit delayed meiotic progression, underscoring the functional importance of MAP7-dependent apical domain formation. Together, these observations define MAP7 as a structural cytoskeletal organizer that coordinates the emergence of the apical domain with timely germ cell maturation.

Results

Localization pattern of MAP7 in Sertoli cells

Map7 is expressed at the mRNA level in both Sertoli and male germ cells (26, 27) ; however, its protein expression and subcellular localization remain uncharacterized. To address this, we generated *Map7-egfp* knock-in (*Map7-egfp*^{KI}) mic (Supplemental Fig. 1A, B). To ensure EGFP tagging did not disrupt MAP7 function, we confirmed homozygous viability and examined MAP7-EGFP^{KI} localization in the fallopian tubes, where MAP7 expression had previously been analyzed using antibodies and *in vivo* electroporation of MAP7-EGFP (18). Homozygous *Map7-egfp*^{KI} mice were viable and fertile (Supplemental Fig. 1C). Consistent with prior observations, MAP7-EGFP^{KI} localized along the planar axis of multiciliated cells on the ovarian (proximal) side of the fallopian tubes (Supplemental Fig. 1D), indicating that EGFP tagging does not interfere with MAP7 function *in vivo*.

We next examined MAP7-EGFP^{KI} localization in adult testes by co-staining with TUBB3, a Sertoli cell-specific β-tubulin isoform. MAP7-EGFP^{KI} colocalized with Sertoli microtubules labeled by TUBB3 (Fig. 1A, top) and exhibited a polarized distribution toward the luminal side (Fig. 1A, top), suggesting a role in microtubule dynamics. Additionally, MAP7-EGFP^{KI} was expressed in step 9–11 spermatids, corresponding to phenotypes observed in *Map7* gene-trap mice (Fig. 1A, bottom), and colocalized with acetylated tubulin, a marker of manchette microtubule (Fig. 1B, bottom). Notably, MAP7-EGFP^{KI} did not colocalize with long-lived stable microtubules outside the manchette (Fig. 1B, top). These localization patterns were further validated using an anti-MAP7 antibody (Fig. 1C). These findings demonstrate that MAP7 specifically localizes to apical microtubules in Sertoli cells and to manchette microtubules in step 9–11 spermatids, underscoring its potential role in microtubule dynamics during spermatogenesis.

MAP7 is essential for the establishment of Sertoli cell polarity and apical domain formation

MAP7 localization in Sertoli cells, along with phenotypes observed in *Map7* gene-trap mice, suggests that MAP7 plays a role in establishing Sertoli cell polarity. However, prior studies used *Map7* gene-trap mice on a mixed B6.129 background, and complete loss of MAP7 protein was not validated (27). To directly assess the role of MAP7 in Sertoli cell polarity, we generated *Map7* knockout (KO) mice on a pure C57BL/6 background (Supplemental Fig. 2A–C). Complete loss of MAP7 protein in homozygous *Map7*$^{-/-}$ mice was confirmed using two independent antibodies (Supplemental Fig. 2D). Consistent with observations in *Map7*

gene-trap mice, *Map7*$^{-/-}$ males exhibited reduced testis size and spermatogenic defects (Supplemental Fig. 2E, F). Notably, the cauda epididymis of *Map7*$^{-/-}$ males contained no mature spermatozoa (Supplemental Fig. 2F), indicating male infertility. Heterozygous *Map7*$^{+/-}$ mice, which showed normal testis size and histology at 8 weeks (Supplemental Fig. 2E, F), were used as controls in subsequent analyses

To examine the temporal dynamics of Sertoli cell polarity establishment, we analyzed seminiferous tubule morphology across the first wave of spermatogenesis, from postnatal day (P)10 to P35. To specifically assess the role of MAP7 in Sertoli cells while minimizing contributions from germ cells, our analysis focused on stages up to P23, before MAP7 expression becomes detectable in step 9–11 spermatids (Fig. 1), to exclude potential secondary effects resulting from MAP7 loss in germ cells. In *Map7*$^{+/-}$ testes, seminiferous tubules were closed at P10, with early primary spermatocytes already evident (Fig. 2A, B). By P15, lumina were present in 13.2% of tubules, increasing to 81.2% by P17, coinciding with the appearance of pachytene spermatocytes. By P21, lumina were detected in 96.7% of tubules and became nearly ubiquitous thereafter (Fig. 2A, B). These findings are consistent with previous reports indicating that Sertoli cell polarization and BTB formation begin around P15–P17, concurrent with pachytene spermatocyte development (28, 29), and suggest that Sertoli cells complete polarity establishment by P21. In contrast, *Map7*$^{-/-}$ tubules appeared morphologically normal at P10 but failed to form lumina between P15 and P28. By P35, multi-lumen structures or abnormally formed lumina were observed (Fig. 2A, B). These observations demonstrate that MAP7 is essential for seminiferous tubule remodeling and implicate it in apical domain formation during Sertoli cell polarization.

Directly assessing Sertoli cell adhesion and morphology is challenging due to the intimate association between Sertoli and germ cells within the seminiferous epithelium. To overcome this, we used serial sectioning and scanning electron microscopy (SEM). In P10 *Map7*$^{+/-}$ mice, 89.3% (25/28) of Sertoli cells adhered to the basement membrane, but only 60.7% (17/28) of Sertoli nuclei were positioned basally (Fig. 2C). By P21, all Sertoli cells adhered (12/12), and 91.7% (11/12) of their nuclei were basal (Fig. 2C). To quantify nuclear positioning in a larger cohort, we performed SOX9 immunostaining. The results showed a similar trend, with basal nuclei increasing to 80.5% from P10 to P17 (Fig. 2D, E; Supplemental Fig. 3A). These findings suggest that at P10, many Sertoli cells exhibit incomplete apical–basal compartmentalization, which progressively matures. Consistent with progressive polarization and lumen formation, Sertoli cells adhering to the basement membrane underwent distinct morphological changes over time (Fig. 2C). In transverse views, Sertoli cells extended apically

from P10 to P21 (Fig. 2C) and elongated along the longitudinal axis, suggesting that Sertoli cell polarity is established along both apical–basal and longitudinal axes during development. In *Map7*$^{-/-}$ mice, Sertoli cell adhesion and nuclear positioning were markedly impaired (Fig. 2C–E; Supplemental Fig. 3A). At P10, 59.5% (22/37) of Sertoli cells adhered to the basement membrane, and only 54.1% (20/37) of their nuclei were basal. By P21, adhesion further decreased, with only 31.6% (6/19) of Sertoli cells attached and 26.3% (5/19) of nuclei basally positioned (Fig. 2C). SOX9 immunostaining revealed a similar trend: the proportion of basal nuclei was 24.9% at P10 and declined to 18.2% at P17 (Fig. 2D, E; Supplemental Fig. 3A), indicating failed apical–basal compartmentalization in *Map7*$^{-/-}$ Sertoli cells. This defect persisted into adulthood (Supplemental Fig. 3B, C). Additionally, in P21 *Map7*$^{-/-}$ mice, Sertoli cells that adhered to the basement membrane failed to elongate in either axis, and apical extension was absent (Fig. 2C), reflecting severe loss of polarity and apical domain formation. In P10 *Map7*$^{+/-}$ mice, luminal F-actin signals were detected but disappeared by P17, coinciding with lumen formation (Fig. 2D; Supplemental Fig. 3A). In contrast, in *Map7*$^{-/-}$ mice, luminal F-actin signals persisted at P17, consistent with histological evidence of closed lumina (Fig. 2D; Supplemental Fig. 3A). These findings suggest that MAP7 is required for actin cytoskeletal remodeling during apical domain formation.

Sertoli cells and male germ cell lineages interact closely within the seminiferous tubules (30-34). To determine whether MAP7 regulates Sertoli cell polarity in a male germ cell lineage-dependent or -independent manner, we examined Sertoli cell nuclear orientation after busulfan-induced depletion of spermatogonial stem cells (SSCs). Busulfan was administered at P28, and testes were analyzed 6 weeks later, after complete elimination of germ cell lineages. Following treatment, *Map7*$^{+/-}$ mice showed testis-to-body weight ratios comparable to untreated *Map7*$^{-/-}$ mice (Supplemental Fig. 3D), and hematoxylin-eosin (HE) staining confirmed germ cell depletion (Fig. 2F; Supplemental Fig. 3E). In *Map7*$^{+/-}$ testes, most Sertoli nuclei remained basally positioned, indicating that once apical–basal polarity is established, it is stably maintained even in the absence of germ cells. In contrast, *Map7*$^{-/-}$ Sertoli nuclei were frequently misoriented toward the lumen under the same conditions (Fig. 2F; Supplemental Fig. 3E), suggesting that polarity defects in *Map7*-deficient Sertoli cells occur independently of germ cell presence.

Collectively, these results demonstrate that MAP7 is indispensable for the establishment of Sertoli cell polarity and apical domain formation. Loss of MAP7 disrupts cytoskeletal remodeling, nuclear positioning, and cell elongation, impairing lumen formation and seminiferous tubule architecture.

MAP7 facilitates microtubule remodeling, but not microtubule stabilization, to establish Sertoli apical domain

Because Sertoli cell polarity is initiated between P10 and P17 and largely completed by P21, we focused on this transition to delineate MAP7-dependent cytoskeletal remodeling. To characterize cytoskeletal remodeling and MAP7 dynamics during this period, we examined microtubules and actin filaments at P10 (prior to polarization) and P17 (during active polarization). At P10, microtubules, actin filaments, and MAP7–EGFP^{KI} signals accumulated on the inner (luminal) side of seminiferous tubules and extended toward the basement membrane (Fig. 3A, top). By P17, these luminal cytoskeletal elements had largely diminished: microtubules became aligned along the luminal–basal axis, and actin filaments reorganized into the basal ES adjacent to the basement membrane (Fig. 3A, bottom). Consistent with our observations in adult testes (Fig. 1A, C), MAP7 exhibited a polarized distribution along microtubules, becoming enriched toward the luminal side at this stage (Fig. 3A, bottom). To assess the native architecture and orientation of apical MAP7-decorated microtubules, we imaged freshly dissected seminiferous tubules from *Map7–egfp*^{KI} mice at P10 and P17. At P10, apical MAP7–EGFP^{KI} signals lacked discernible directionality and appeared randomly oriented (Fig. 3B, left). By P17, MAP7-decorated apical microtubules displayed a consistent longitudinal alignment along the tubule axis (Fig. 3B, right). This developmental transition parallels our array-tomography findings showing that apical processes elongate and adopt a longitudinal orientation between P10 and P21 (Fig. 2C). Together, these results demonstrate that cytoskeletal remodeling—including luminal MAP7 accumulation and the emergence of directional organization within the apical microtubule network—occurs after P10, coinciding with the onset of Sertoli cell polarization.

We next examined the impact of *Map7* deletion on cytoskeletal remodeling during Sertoli cell polarization. In *Map7*$^{+/-}$ mice at P17, microtubules on the inner side of the tubules, which were prominent at P10, were lost, and actin filaments had relocated to form the basal ES (Fig. 4A, top). In contrast, in *Map7*$^{-/-}$ mice at P17, inner microtubule signals persisted, resembling the P10 pattern in controls, and although staining intensity was preserved, microtubule alignment along the luminal–basal axis was disrupted (Fig. 4A, bottom). Similarly, actin filaments remained abnormally accumulated on the luminal side (Fig. 4A, bottom). These findings indicate that Sertoli cells lacking MAP7 fail to transition beyond a P10-like cytoskeletal organization, highlighting the essential role of MAP7 in orchestrating microtubule alignment and cytoskeletal remodeling during polarization. Consistent with these observations

at P17, 8-week-old *Map7*$^{-/-}$ testes retained similar defects. In *Map7*$^{+/-}$ mice, Sertoli microtubules extended along the luminal–basal axis, and apical actin filaments formed the ES normally (Supplemental Fig. 4A, top). In *Map7*$^{-/-}$ mice, although microtubule staining intensity was preserved, alignment remained disrupted, and apical actin filaments were replaced by ectopic structures (Supplemental Fig. 4A, bottom). These results suggest that MAP7 primarily promotes microtubule alignment rather than stabilization, thereby organizing the cytoskeletal framework throughout maturation.

Since cytoskeletal organization is essential for apical domain formation, we examined whether MAP7 is required for the assembly of Sertoli cell junctional structures. In the testis, tight junctions reside at the basal side of Sertoli cells and contribute to BTB formation, partitioning the seminiferous epithelium into basal and luminal compartments. We then performed SEM to examine the effects of *Map7* KO. In P21 *Map7*$^{+/-}$ testes, electron-dense regions along the basal side of Sertoli–Sertoli junctions corresponded to tight junctions closely associated with the endoplasmic reticulum, consistent with previous reports (35) (Fig. 4B; Supplemental Fig. 4B). The region immediately apical to the tight junctions likely represents adherens junctions, which were also associated with the endoplasmic reticulum. Unlike tight junctions, these regions displayed wider intercellular spaces, reflecting the looser membrane apposition typical of adherens junctions, though they could not be definitively distinguished from gap junctions or desmosomes based on morphology alone (Fig. 4B; Supplemental Fig. 4B). At P10, both *Map7*$^{+/-}$ and *Map7*$^{-/-}$ testes lacked clearly defined tight junctions and adherens junction–like structures (Fig. 4B; Supplemental Fig. 4B). In P21 *Map7*$^{-/-}$ mice, Sertoli cells formed expanded basal tight junctions but failed to establish adherens junction–like structures (Fig. 4B; Supplemental Fig. 4B). Consistent with these ultrastructural findings, ZO-1, a tight junction marker, localized specifically to the basal ES, marked by F-actin, in *Map7*$^{+/-}$ testes (Fig. 4C, D). In *Map7*$^{-/-}$ testes, ZO-1 mislocalized to ectopic F-actin-rich regions (Fig. 4C, D). β-catenin, a core adherens junction component, colocalized with F-actin at junctional regions near the basal ES in *Map7*$^{+/-}$ testes (Fig. 4A; Supplemental Fig. 4A). In *Map7*$^{-/-}$ testes, β-catenin accumulated on the luminal side, reflecting mislocalization of actin and microtubules (Fig. 4A; Supplemental Fig. 4A). Together, these results show that MAP7-dependent microtubule remodeling coordinates cytoskeletal architecture and junctional complex assembly, enabling apical domain formation during Sertoli cell polarization.

MAP7 coordinates microtubules with actomyosin-associated regulators during Sertoli cell polarization.

MAP7 promotes microtubule remodeling during Sertoli cell polarization, potentially by coordinating broader cytoskeletal organization. To explore the molecular basis underlying this activity, we identified proteins associated with MAP7 using comparative immunoprecipitation-mass spectrometry (IP-MS). Two datasets were analyzed: *MAP7-egfp*^{KI} HeLa cells (Fig. 5A) and testes from P17–P20 *Map7-egfp*^{KI} mice (Fig. 5B). *MAP7-egfp*^{KI} HeLa cells provided a complementary system with sufficient material for robust proteomic profiling. Proteins detected in both systems likely represent general MAP7-associated factors, whereas those enriched specifically in testes may reflect functions relevant to polarizing Sertoli cells. The kinesin-1 heavy chain KIF5B, a known MAP7-associated motor, was detected in both datasets, supporting the validity of our approach (Fig. 5A-C). Comparative analysis identified 22 proteins selectively enriched in MAP7 IP from P17–P20 testes (Fig. 5C). Metascape analysis revealed overrepresented categories including motor proteins and Rho GTPase effectors (Fig. 5D). Among these, we focused on cytoskeletal regulators (Fig. 5E), such as TUBB3, NMII heavy chains MYH9/MYH10, and vimentin (VIM), consistent with a role for MAP7 in coordinating multiple cytoskeletal systems.

We prioritized MYH9 for further study due to its strong enrichment and established role in cytoskeletal remodeling. We examined MYH9 localization during Sertoli cell polarization and its dependence on MAP7. Remarkably, MYH9 was selectively enriched at luminal regions where microtubules and F-actin co-localized but was absent from areas lacking either component (Fig. 5F; Supplemental Fig. 5), revealing a distinctive apical accumulation pattern during polarization. In *Map7*$^{-/-}$ testes, microtubule and F-actin structures persisted in luminal regions where they are typically cleared during polarization; however, MYH9 failed to localize to these ectopic domains and instead remained diffusely distributed in the cytoplasm (Fig. 5G; Supplemental Fig. 5). These findings indicate that MYH9 localization at the luminal interface depends on MAP7, and suggest that MAP7 helps coordinate microtubules and F-actin, potentially via its association with NMII heavy chains.

Functional differentiation of Sertoli cells is largely preserved in the absence of MAP7

We showed that MAP7-mediated cytoskeletal remodeling establishes the Sertoli apical domain, which provides a structural scaffold for seminiferous epithelium organization. To determine whether loss of MAP7 affects functional differentiation of Sertoli cells, we performed scRNA-Seq at P19. GFP-positive Sertoli cells were isolated using a *Sox9-ires-gfp* allele and fluorescence-activated cell sorting (FACS) (Supplemental Fig. 6A). Despite efficient dissociation and 10x Genomics library preparation, low-level germ cell contamination was

detected; therefore, Sertoli cell–specific transcriptomes were extracted based on expression of *Gata4*, *Sox9*, *Kitl*, and *Dhh*, yielding 311 control and 434 *Map7*$^{-/-}$ Sertoli cells (Supplemental Fig. 6B).

UMAP clustering identified six transcriptionally distinct clusters (C0–C5) (Fig. 6A). Gene set enrichment analysis (Metascape) revealed functional specialization among these clusters (Fig. 6B; Supplemental Fig. 7). C0 was enriched for pathways associated with chemical stress responses, highlighting a multifaceted protective state. C1 showed upregulation of fructose metabolism genes, consistent with a metabolically active population with enhanced mitochondrial and antioxidant capacity. C2 expressed polarity-associated genes, representing a dynamic state responsive to signals in the spermatogenic niche. C3 was enriched for cytoskeletal and TGFβ-associated pathways, implicating it in ECM remodeling and proliferation control. C4 expressed ECM-related genes, suggesting a structurally specialized subtype involved in BTB maintenance. C5 co-upregulated stress-response and carbon metabolism genes, indicating a high-energy, stress-adapted state supporting spermatogenesis.

To reconstruct differentiation trajectories among these clusters, we applied Monocle3, which infers pseudotime using graph-based, branch-aware topology. C1 was selected as the root based on shared specificity and entropy scores, consistent with its metabolically active and transcriptionally diverse profile (Fig. 6B, C; Supplemental Fig. 7). Median pseudotime ordering revealed a clear and continuous maturation sequence in controls (C1 → C5 → C3 → C0 → C4 → C2) (Fig. 6D). In *Map7*$^{-/-}$ Sertoli cells, early cluster ordering was shifted: C5 and C4 occupied the lowest pseudotime values, and the original control root cluster C1 appeared at an intermediate stage (Fig. 6D). Although C2 remained the terminal state in both genotypes, the pseudotime gap between C0 and C2 was reduced, suggesting a mild compression of late-stage progression. Importantly, these shifts in pseudotime do not reflect structural disruptions of the differentiation landscape (Fig. 6C). The Monocle3 principal graphs showed nearly identical average node degrees between genotypes (Fig. 6C), indicating preservation of neighborhood structure and local cellular connectivity. Differences in branch points and graph diameter were minimal and did not produce additional branches or alternative trajectories in *Map7*$^{-/-}$ cells (Fig. 6C). Moreover, the relative proportions and spatial distribution of the six transcriptionally defined clusters remained similar, and no aberrant or novel cell states emerged (Fig. 6A, E). Together, these findings indicate that MAP7 is not required to establish the global topology of Sertoli cell differentiation. Rather, its loss induces subtle shifts in the relative positioning of clusters along pseudotime, consistent with minor delays or compression in specific maturation transitions without altering the overall differentiation architecture.

Sertoli apical domain ensures orderly progression through the pachytene stage during meiosis

Our analyses showed that MAP7 coordinates the remodeling of microtubule and actin networks and regulates the formation of junctional structures. While MAP7 is essential for apical domain formation and its disruption alters specific aspects of Sertoli cell function, the overall functional differentiation of Sertoli cells is largely preserved in its absence. Sertoli cell adhesion generates the stem cell niche for SSCs (36, 37). To assess this further, we quantified SSCs in 8-week-old *Map7*$^{+/-}$ and *Map7*$^{-/-}$ mice. GFRα1^{+} SSCs were not reduced in *Map7*$^{-/-}$ mice compared to those in *Map7*$^{+/-}$ controls (Fig. 7A, B), suggesting that Sertoli cells can still support the SSC niche despite the loss of adherens junctions, gap junctions, and apical domain, provided tight junctions are present. We next examined spermatogenic progression in 8-week-old *Map7*$^{+/-}$ and *Map7*$^{-/-}$ mice using ZFP541, a marker expressed from pachytene spermatocytes to round spermatids. Cell populations were quantified based on nuclear morphology and SYCP3 co-expression. In *Map7*$^{-/-}$ testes, both pachytene spermatocytes and round spermatids were reduced, with a more pronounced decrease in round spermatids (Fig. 7C, D; Supplemental Fig. 8A). To determine whether this reduction was due to increased cell death, we performed TUNEL staining. No apoptotic cells were observable in either genotype Supplemental Fig. 8B), indicating that round spermatid reduction cannot be attributable to cell death but instead suggests delayed differentiation into the round spermatid stage.

To assess the impact of apical domain disruption on germ cell development, we performed scRNA-Seq at P23, a stage preceding the appearance of step 9–11 spermatids (Supplemental Fig. 8C). This timing enabled focused analysis on earlier spermatogenic populations. At this stage, phenotypes observed in *Map7*$^{-/-}$ testes, including luminal closure, abnormal microtubule organization, and ectopic accumulation of F-actin and β-catenin, remained evident (Supplemental Fig. 8C, D). We dissociated whole testes from *Map7*$^{+/-}$ and *Map7*$^{-/-}$ mice and performed scRNA-Seq using the 10x Genomics platform. Germ cells were identified by *Ddx4* expression, yielding 1,914 *Map7*$^{+/-}$ and 4,745 *Map7*$^{-/-}$ germ cells (Supplemental Fig. 9). After dataset integration and unsupervised clustering, we identified 15 clusters (clusters 0–14; Supplemental Fig. 10A). To define germ cell differentiation stages, we used stage-specific marker analysis and RNA velocity profiling (Supplemental Fig. 10B, C). Metascape analysis revealed distinct biological processes enriched in each cluster, aligned with the expected progression of spermatogenesis (Supplemental Fig. 11). Based on inferred trajectory positions, clusters were renamed Ca–Co to reflect their differentiation order (Fig. 7E;

Supplemental Fig. 10A). We then quantified the proportion of cells in each cluster to assess genotype-specific changes. To determine whether cluster expansion reflected aberrant meiotic entry, we examined expression of *Stra8* and *Meiosin*, key meiotic inducers (38). Both genes were appropriately upregulated at meiotic entry and downregulated thereafter in *Map7*$^{-/-}$ germ cells, consistent with *Map7*$^{+/-}$ controls (Supplemental Fig. 12A). STRA8 protein levels were similarly unchanged between genotypes (Supplemental Fig. 12B), indicating that meiotic initiation and early transcriptional programs remained intact. Despite appropriate meiotic entry, cytological assessment showed delayed progression in *Map7*$^{-/-}$ testes, with significantly fewer seminiferous tubules containing round spermatids compared to *Map7*$^{+/-}$ controls (Supplemental Fig. 12C, D). Consistent with this delay, cluster-level quantification revealed a marked expansion of clusters Cg and Ci in *Map7*$^{-/-}$ testes (Fig. 7F). In addition, clusters Cf–j exhibited transcriptional silencing of sex-chromosomal genes (Fig. 7F), indicating that these populations had progressed at least to the pachytene stage. To further resolve the identity of the expanded clusters Cg and Ci, we analyzed the expression of *Prelid1* and *Ccna1*, which mark early and late pachytene stages, respectively. *Prelid1* is expressed through early pachytene, and its downregulation marks the transition to mid-pachytene (39), whereas *Ccna1* expression increases during late pachytene and remains high into diplotene (40). *Prelid1* expression extended through Cg, indicating that Cg represents early pachytene cells expanded in *Map7*$^{-/-}$ testes (Fig. 7G). *Ccna1* was elevated in Ci of *Map7*$^{-/-}$ testes, whereas in *Map7*$^{+/-}$ testes, it was restricted to Cj, identifying Ci as a late pachytene population unique to *Map7*$^{-/-}$ mice. Notably, trajectory inference indicated that the Ci cluster in *Map7*$^{-/-}$ testes progresses to Ck (diplotene) through an alternative route that bypasses the Cj stage, as observed in *Map7*$^{+/-}$ mice (Fig. 7G). Together, these findings demonstrate that the Sertoli apical domain is essential for guiding orderly progression through the pachytene stage of meiosis.

Discussion

We identify MAP7 as a central regulator of Sertoli cell polarity and apical domain formation, addressing a long-standing gap in understanding how microtubules are dynamically reorganized during epithelial polarization in the early postnatal testis. Although the importance of Sertoli cell polarity for testicular architecture and germ cell development is well established (1), the nature of microtubule remodeling during this process has remained largely unexplored. Using a *Map7–egfp*^{KI} allele, we show that MAP7 becomes enriched on apical microtubules precisely during the period when Sertoli cells acquire polarity, and is required for their dynamic reorganization. Rather than stabilizing microtubules, MAP7 supports the rearrangements necessary to assemble the apical domain and organize the distribution of F-actin. Proteomic analyses identified MYH9 and MYH10 among MAP7-associated proteins in polarizing Sertoli cells, suggesting that MAP7 contributes to the cytoskeletal environment in which microtubule and actomyosin structures are spatially coordinated during epithelial maturation. Consistent with this, MAP7 loss disrupts cytoskeletal organization, alters epithelial morphology, impairs adherens and gap junction assembly, and causes ectopic expansion of tight junctions—a constellation of defects that corresponds with the failure of lumen formation during the first wave of spermatogenesis.

We further found that MYH9 becomes enriched at luminal regions where apically remodeled microtubules and F-actin converge—a spatial organization absent in *Map7*$^{-/-}$ Sertoli cells. In the KO, both microtubules and F-actin are markedly disorganized, yet they still accumulate within the region that would normally give rise to the lumen. Despite this positional convergence, MYH9 fails to become enriched at these ectopic sites. Because the cytoskeletal architecture at these locations differs substantially from that in controls, these observations suggest that MAP7 is required to generate the apical cytoskeletal conditions that normally accompany NMII enrichment, without implying a specific sequence of events. Spatially restricted NMII enrichment has been described in several epithelia: NMII accumulates apically in the nephric duct and ureteric bud to support epithelial constriction and adhesion (41), and apical MYH9 contributes to coordinated cell movements during dental epithelial invagination (42). The absence of analogous apical MYH9 enrichment in *Map7*$^{-/-}$ Sertoli cells—even at sites where microtubules and F-actin converge—supports the interpretation that MAP7 is necessary to establish the structural context within which NMII becomes apically enriched during apical domain assembly. Although the molecular cues governing NMII localization remain to be determined, the phenotypes associated with MAP7 loss underscore its importance in shaping the cytoskeletal environment required for this enrichment.

Our findings extend previous work implicating actin regulators such as RAC1 and CDC42 in Sertoli cell polarity by demonstrating that microtubule remodeling represents a complementary and indispensable dimension of epithelial patterning (4, 5). Whereas earlier studies emphasized actin-based mechanisms, our identification of MAP7-dependent microtubule remodeling as a requirement for apical domain formation adds an additional layer to cytoskeletal organization. In *Map7*$^{-/-}$ Sertoli cells, adherens and gap junctions are markedly diminished while tight junctions are ectopically expanded, reflecting an imbalance in junctional composition and spatial organization. Because proper BTB formation relies on the coordinated positioning of multiple junction types, such structural disorganization may not recreate the architectural conditions typically associated with normal barrier assembly. These observations place MAP7-dependent microtubule remodeling upstream of junctional organization and epithelial compartmentalization.

Sertoli cells form the SSC niche through BTB construction and secretion of trophic factors (36, 37). Although polarity loss has been linked to impaired niche function, our data show that in *Map7*$^{-/-}$ Sertoli cells, tight junctions persist but form ectopically, while adherens junctions fail to assemble. Despite these abnormalities, SSC numbers remain unchanged over eight weeks, and the first wave of spermatogenesis proceeds without overt defects in spermatogonial differentiation. These findings suggest that tight junctions—despite their mislocalization—may be sufficient to support early spermatogenesis, and that canonical apical domain architecture is not essential for SSC maintenance during the postnatal period. Furthermore, after germ cell depletion by busulfan treatment, *Map7*$^{-/-}$ Sertoli cells fail to restore basal nuclear positioning, indicating that MAP7 acts cell-autonomously in Sertoli cells to establish and maintain polarity, rather than through germ cell–dependent mechanisms.

Our scRNA-seq analyses show that despite severe defects in polarity and apical domain formation, the intrinsic transcriptional differentiation programs of Sertoli cells are largely preserved in *Map7*$^{-/-}$ mice. This suggests that MAP7 influences spatial and structural organization rather than core cellular identity. Thus, the apical domain may regulate germ cell development primarily through its spatial architecture, consistent with the delayed meiotic progression observed in *Map7*-deficient testes. This delay occurs without increased apoptosis or defects in meiotic initiation, implicating the apical domain as a structural niche component that helps ensure timely meiotic progression. Given the reliance of germ cells on Sertoli-derived organizational and trophic support, our findings suggest that microtubule-driven apical remodeling governs key intercellular interactions required for germ cell differentiation.

Together, our results identify MAP7-dependent microtubule remodeling as a key

organizing element for Sertoli cell polarity and for generating the epithelial architecture required for male germ cell differentiation. By integrating *in vivo* genetics, quantitative imaging, and single-cell transcriptomics, this study demonstrates that MAP7 provides the spatial cytoskeletal framework that enables Sertoli cells to establish an apical domain, maintain junctional configuration, and support meiotic progression. Notably, MAP7 acts without altering Sertoli cell identity or global transcriptional programs, indicating that microtubule architecture constitutes a decisive regulatory layer governing niche function. These findings reveal a previously underappreciated mode of cytoskeletal organization in a vertebrate stem cell–supporting epithelium and establish MAP7 as a critical determinant of the structural logic that underpins spermatogenic output. More broadly, this work shows how microtubule-driven polarity cues can operate as an autonomous organizing mechanism in highly specialized epithelia, offering a conceptual framework applicable across systems without requiring mechanistic extrapolation.

Materials and Methods

Animals

C57BL/6NJcl mice were purchased from CLEA Japan (Tokyo, Japan). We used *Map7*$^{+/-}$, *Sox9-ires-gfp;Map7*$^{+/-}$, and *Map7-egfp*^{KI} mice, all maintained on a C57BL/6 background, for this study. The *Sox9-ires-gfp* mouse line was originally generated by Nel-Themaat *et al*. (43). For scRNA-Seq of total testis cells, *Map7*$^{+/-}$ or *Map7*$^{-/-}$ male mice at P23 were used. For scRNA-Seq targeting Sertoli cells, *Sox9-ires-gfp* or *Sox9-ires-gfp; Map7*$^{-/-}$ male mice at P19 were used. Testes collected from mice at P10–P35 and at 8 weeks of age were used for histological and immunostaining analyses. Whenever possible, KO animals were compared with littermates or age-matched non-littermate controls from the same colony, unless otherwise specified. Mice were housed under standard conditions in a temperature- and light-controlled facility (12-hour light/dark cycle; 22□±□1□°C). All animal procedures were approved by the Institutional Animal Care and Use Committee (approval numbers: A2019-127, A2021-018, A2023-036, and A2025-018) and conducted in accordance with institutional guidelines.

Cell culture

Wild-type and *MAP7-EGFP*^{KI} HeLa cells were cultured in Dulbecco's Modified Eagle Medium (DMEM, 043-30085; Fujifilm Wako Pure Chemical, Osaka, Japan) supplemented with 10% fetal bovine serum (FBS, 35-015-CV; Corning, Corning, NY, USA) and penicillin–streptomycin (26253-84; Nacalai, Kyoto, Japan) at 37 °C in a humidified atmosphere containing 5% CO□ (18).

crRNAs and genotyping primers

The sequences of crRNAs and genotyping primers used in this study are provided in Supplemental Tables 1 and 2, respectively.

Generation of *Map7*$^{+/-}$ mice and genotyping

Map7$^{+/-}$ mice were generated by introducing Cas9 protein (317-08441; NIPPON GENE, Toyama, Japan), tracrRNA (GE-002; FASMAC, Kanagawa, Japan), and synthetic crRNA (FASMAC) into C57BL/6N fertilized eggs via electroporation. To generate the *Map7* exon2–8 deletion (Ex2-8Δ) allele, synthetic crRNAs were designed to target the sequences GGACAAACTAGCAACCACTC(AGG) in exon 2 and CGCCTGAGGGCTCTGCACGA(AGG) in exon 8 of the *Map7* gene.

The electroporation mixture consisted of tracrRNA (10 μM), synthetic crRNA (10 μM), and Cas9 protein (0.1 μg/μL) in Opti-MEM I Reduced Serum Medium (31985062; Thermo Fisher Scientific, Waltham, MA, USA). Electroporation was performed using the Super Electroporator NEPA 21 (NEPA GENE, Chiba, Japan) on glass microslides with round wire electrodes (1.0 mm gap, 45-0104; BTX, Holliston, MA, USA). The procedure included four steps of square-wave pulses: (1) three poring pulses of 3 ms each at 30 V with 97 ms intervals; (2) three polarity-reversed poring pulses of 3 ms each at 30 V with 97 ms intervals; (3) five transfer pulses of 50 ms each at 4 V with 50 ms intervals and 40% decay in voltage per pulse; and (4) five polarity-reversed transfer pulses of 50 ms each at 4 V with 50 ms intervals and 40% decay in voltage per pulse.

The targeted *Map7* Ex2-8Δ allele in F0 mice was identified via PCR using the following primers: *Map7*_C1F (5′-TAATGCAGGACCAGTCACTCTGCTGAACAG-3′) and *Map7*_C2R (5′-CTGTCACCTGATCTTGTACCCA-3′) for the KO allele (366 bp); *Map7*_C1F and *Map7*_C1R (5′-TAAGAACAGTAACTGCCCTTGCAGAGGACC-3′) for the exon 2 of the wild-type allele (597 bp); or Map7_C2F (5′-ACCTGCACTCTAGTTATCCCCA-3′) and *Map7*_C2R for the exon 8 of the wild-type allele (228 bp). PCR amplicons were confirmed using Sanger sequencing. Genotyping PCR was routinely performed as follows. Genomic DNA was prepared by incubating a small piece of the cut toe in 180 μL of 50 mM NaOH at 95 °C for 15 min, followed by neutralization with 20 μL of 1 M Tris-HCl (pH 8.0). After centrifugation for 20 min, 1 μL of the resulting DNA solution was used as the PCR template. Each reaction (8 μL total volume) contained 4 μL of Quick Taq HS DyeMix (DTM-101; Toyobo, Osaka, Japan) and a primer mix. PCR cycling conditions were as follows: 94 °C for 2 min; 35 cycles of 94 °C for 30 s, 65 °C for 30 s, and 72 °C for 1 min; followed by a final extension at 72 °C for 2 min and a hold at 4 °C. PCR products were analyzed using agarose gel electrophoresis. This protocol was also applied to other mouse lines and alleles generated in this study.

Generation of *Map7-egfp* knock-in mice and genotyping

Map7-egfp^{KI} mice were generated using the PITCh system, as previously described (44). Cas9 protein, tracrRNA, synthetic crRNA, and the PITCh vector were introduced into C57BL/6N fertilized eggs via electroporation. The synthetic crRNA was designed to target the sequence ACTCATATAACTTCTACATG(AGG) within the Map7 gene and GTGCTTCGATATCGATCGTT(TGG) within the PITCh vector.

The targeted *Map7-egfp*^{KI} allele in F0 mice was identified by PCR using the following primers: *Map7-egfp*_C1F (5′-CTGACCTGTTCTTCCTACAGCA-3′) and *Map7-egfp*_C1R

(5′-AGCCTGAAGTTCCATTCATTGT-3′) to amplify both the *Map7-egfp*^{KI} allele (996 bp) and the wild-type allele (228 bp). To confirm 5′ integration of the *Map7-egfp*^{KI} allele, primers *Map7-egfp*_C1F and *Map7-egfp*_E1R (5′-TTGTACAGCTCGTCCATGCCGAG-3′) were used to amplify a 935 bp fragment; for 3′ integration, *Map7-egfp*_E1F (5′-ACCACATGAAGCAGCACGACTTC-3′) and *Map7-egfp*_C1R were used to amplify a 548 bp fragment. All PCR amplicons were confirmed by sequencing.

Immunoblotting

For immunoblotting, testes were lysed in Laemmli sample buffer prepared in-house. After boiling, the lysates were separated by SDS–PAGE, transferred to polyvinylidene difluoride (PVDF) membranes (MilliporeSigma, Burlington, MA, USA), and immunoblotted with antibodies. Detection was performed using Amersham ECL Prime (RPN2236; Cytiva, Tokyo, Japan), and signals were visualized using the FUSION Solo imaging system (Vilber Lourmat, Marine, France). The following primary antibodies were used: mouse anti-Actin (C4, 0869100-CF; MP Biomedicals, Irvine, CA, USA), mouse anti-Clathrin heavy chain (610500; BD Biosciences, Franklin Lakes, NJ, USA), rat anti-GFP (GF090R; Nacalai, 04404-84), rabbit anti-MAP7 (SAB1408648; Sigma-Aldrich, St. Louis, MO, USA), rabbit anti-MAP7 (C2C3, GTX120907; GeneTex, Irvine, CA, USA), and mouse anti-α-tubulin (DM1A, T6199; Sigma-Aldrich). Corresponding HRP-conjugated secondary antibodies were used for detection: goat anti-mouse IgG (12-349; Sigma-Aldrich), goat anti-rabbit IgG (12-348; Sigma-Aldrich), and goat anti-rat IgG (AP136P; Sigma-Aldrich). Detailed information for all primary and secondary antibodies is provided in Supplemental Table 3.

Histological analysis

For HE staining, testes and epididymides were fixed in 10% neutral buffered formalin or in-house–prepared Bouin's solution, followed by paraffin embedding. Sections were cut at a thickness of 6 μm and mounted on CREST-coated glass slides (SCRE-01; Matsunami Glass, Osaka, Japan). After dehydration, sections were stained with HE using standard protocols.

For immunofluorescence, testes were fixed overnight at 4 °C in 4% paraformaldehyde in PBS, then cryoprotected by immersion in 10%, 20%, and 30% sucrose solutions at 4 °C. Tissues were briefly incubated in OCT compound (4583; Sakura Finetechnical, Tokyo, Japan) at room temperature, embedded in OCT, and snap-frozen in liquid nitrogen. Cryosections (10 μm thick) were stored at −80 °C until use. Prior to staining, sections were washed once in PBS for 10 min and twice in 0.1% Triton X-100/PBS for 10 min each. Blocking was performed using

2.5% normal donkey serum (017-000-121; Jackson ImmunoResearch Laboratories, PA, USA) and 2.5% normal goat serum (005-000-121; Jackson ImmunoResearch Laboratories) in 0.1% Triton X-100/PBS for 1 h at room temperature. Sections were incubated with primary antibodies overnight at 4 °C and subsequently with Alexa Fluor-conjugated secondary antibodies (Thermo Fisher Scientific) for 1 h at room temperature. Detailed information on all primary and secondary antibodies is provided in Supplemental Table 3. For PNA lectin and phalloidin staining, FITC-conjugated *Arachis hypogaea* lectin (1:1000, L7381; Sigma-Aldrich) and Alexa Fluor 647-conjugated phalloidin (1:1000, A2287; Thermo Fisher Scientific) were used, respectively. TUNEL staining was performed using the MEBSTAIN Apoptosis TUNEL Kit Direct (8445; MBL, Tokyo, Japan) to detect apoptotic cells. Nuclei were counterstained with DAPI (D9542; Sigma-Aldrich) for 30 min at room temperature. Imaging was performed using a Leica TCS SP8 confocal microscope, and images were processed using LAS X software (version 2, Leica Microsystems, Vienna, Austria). Objectives used were HC PL APO 40×/1.30 OIL CS2 (11506428; Leica) and HC PL APO 63×/1.40 OIL CS2 (11506350; Leica), with digital zoom applied as needed for high-magnification imaging. DAPI was detected using PMT detectors, while Alexa Fluor 488, 594, and 647 signals were captured using HyD detectors. Images were acquired in sequential mode with detector settings adjusted to prevent signal bleed-through. Laser power and exposure settings were optimized for each experiment but kept constant during acquisition to ensure comparability across samples. Image brightness was adjusted linearly within a consistent dynamic range using Fiji software (v.2.16/1.54p; NIH) (45). For Fig. 7D, cell quantification was performed using Aivia software (version 14.1; Leica). Statistical analyses and graph generation were performed using Microsoft Excel (Microsoft Office LTSC Professional Plus 2021), except for ANOVA, which was conducted in R (version 4.4.0) (46). For ANOVA, linear models were fitted using the base **stats** package (lm function), and analysis of variance was performed with the **anova** function.

Volume electron microscopy (array tomography)

Immediately following euthanasia, testes were dissected from animals, immersed in half-strength Karnovsky fixative (2% paraformaldehyde, 2.5% glutaraldehyde in 0.1 M phosphate buffer, pH 7.3), bisected in fixative, and fixed for 48 h. The tissue was post-fixed with 1% osmium tetroxide in buffer, dehydrated in a graded ethanol series, and embedded in EPON 812 resin using TAAB Embedding Resin Kit with DMP-30 (T004; TAAB Laboratory and microscopy, Berks, UK). After trimming to a 0.5 mm square, approximately 600 serial 50 nm ultrathin sections were collected on silicon wafers. Sections were stained with uranyl acetate

and modified Sato's lead solution (47) for 5 min each and subjected to SEM (JSM-IT800SHL; JEOL, Tokyo, Japan) to generate a stack of serial section images. Imaging was conducted at a pixel resolution of 5 nm × 5 nm, with two montaged images per section, each at 7680 × 5760 pixels. After alignment using Stacker Neo (version 3.5.3.0; JEOL), 1/2 or 1/4 binning was applied. Three-dimensional ultrastructural visualization and analysis were performed using Amira 2022 (version 2022.1; Thermo Fisher Scientific) and Microscopy Image Browser (version 2.91) (48). For Fig.3C, regions of interest within the image stack were subsequently re-examined at a higher pixel resolution of 1.25 nm × 1.25 nm.

Confocal imaging of MAP7-EGFP^{KI} in living seminiferous tubules

Seminiferous tubules were freshly dissected from P10 or P17 *Map7-egfp^{KI}* mice and dissociated in PBS. Individual tubules were immediately transferred to 35 mm glass-bottom dishes (D11130H; Matsunami) for imaging. Focusing on the apical side allowed visualization of MAP7-EGFP^{KI} localization in its native orientation. Confocal imaging was performed using a Leica TCS SP8 microscope equipped with an HC PL APO 63×/1.40 OIL CS2 objective (11506350; Leica). Digital zoom was applied as necessary to achieve high-magnification images. GFP signals were detected using HyD detectors under standard settings.

Immunoprecipitation

Wild-type and *MAP7-egfp^{KI}* HeLa cells were lysed in a buffer containing 10 mM Tris-HCl (pH 7.5), 150 mM NaCl, 0.5 mM EDTA, and 0.5% NP-40, supplemented with complete protease inhibitor (4693116001; Roche Diagnostics, Mannheim, Germany). Testes were harvested from male C57BL/6 wild-type or *Map7-egfp^{KI}* mice at P17–P20, detunicated, and homogenized in the same lysis buffer with protease inhibitors. Lysates were cleared by centrifugation at 100,000 × *g* for 10 min at 4 °C. To reduce nonspecific interactions, supernatants were precleared through incubation with 50 μL of ChromoTek control magnetic agarose beads (bmab; Proteintech, Rosemont, IL, USA) for 1 h at 4 °C with gentle rotation. The resulting supernatants were used as input material for immunoprecipitation. To isolate Map7/MAP7-EGFP^{KI} complexes, 50 μL of ChromoTek GFP-Trap magnetic agarose beads (gtma; Proteintech) were added to the lysates. After incubation, the beads were washed thoroughly with lysis buffer, and bound proteins were eluted with 40 μL of elution buffer (100 mM Glycine-HCl, pH 2.5, 150 mM NaCl) and neutralized with 4 μL of 1 M Tris-HCl (pH 8.0).

Mass spectrometry

Immunoprecipitated proteins were separated on 4–12% NuPAGE gels (NP0321PK2; Thermo Fisher Scientific) and electrophoresed until they migrated approximately 1 cm from the loading wells. Gels were stained with SimplyBlue SafeStain (LC6060; Thermo Fisher Scientific), and protein-containing bands were excised and diced into approximately 1 mm pieces. Gel fragments were subjected to in-gel digestion: proteins were reduced with dithiothreitol (DTT; Thermo Fisher Scientific), alkylated with iodoacetamide (Thermo Fisher Scientific), and digested overnight at 37 °C using trypsin and Lysyl endopeptidase (Promega, Madison, WI, USA) in 40 mM ammonium bicarbonate buffer (pH 8.0).

The generated peptides were analyzed using an Advanced UHPLC system (ABRME1ichrom Bioscience) coupled to a Q Exactive mass spectrometer (Thermo Fisher Scientific). Raw data were acquired using Xcalibur software (version 4.0.27.19; Thermo Fisher Scientific) and processed using Proteome Discoverer version 1.4 (Thermo Fisher Scientific) in combination with Mascot version 2.5 (Matrix Science, Boston, MA, USA). Searches were conducted against the SwissProt database (49), restricted to entries for *Homo sapiens* or *Mus musculus*. A decoy database comprising randomized or reversed sequences was used to estimate the false discovery rate (FDR), and peptide identification confidence was evaluated using the Percolator algorithm. Peptide-spectrum matches were filtered to maintain a global FDR below 1%, ensuring high-confidence identifications. The complete LC-MS/MS dataset has been deposited in jPOST (50) under the accession numbers PXD066392 (ProteomeXchange) and JPST003958 (jPOST).

scRNA-Seq

Testes were isolated from *Sox9-ires-gfp* and *Sox9-ires-gfp;Map7*$^{-/-}$ mice at P19, or from *Map7*$^{+/-}$ and *Map7*$^{-/-}$ mice at P23. The tissue was finely minced and digested with 1.2 mg/mL type I collagenase (Fujifilm Wako Pure Chemical) at 37 °C for 10 min, followed by centrifugation to collect tissue pellets. Pellets were incubated with Accutase (Innovative Cell Technologies, San Diego, CA, USA) for 5 min at 37 °C. The digestion was terminated by adding DMEM supplemented with 10% FBS, and the resulting cell aggregates were gently dissociated by pipetting. Cell suspensions were sequentially passed through 95 μm and 35 μm strainers (BD Biosciences, Milpitas, CA, USA) to remove debris and large clumps. Cells were pelleted by centrifugation, resuspended in PBS containing 0.1% bovine serum albumin, and sorted using a SH800 cell sorter (SONY, Tokyo, Japan) to exclude dead cells. GFP-positive cells were isolated for Sertoli cell-specific scRNA-Seq. Viable cells were resuspended in DMEM with 10% FBS. Approximately 7,000 single cells were loaded onto a Chromium controller (10x Genomics,

Pleasanton, CA, USA) for droplet-based single-cell capture. Libraries were prepared using the Chromium Single Cell 3 Reagent Kits v3 (PN-1000075; 10x Genomics), following the manufacturer's protocol, and sequenced on an Illumina HiSeq X platform to generate 150 bp paired-end reads. Details on the number of mice used, total cells captured, mean reads per cell, sequencing saturation, number of genes detected per cell, median UMI counts per cell, and total cell numbers before and after quality control are provided in Supplemental Fig. 6B and Supplemental Fig. 9A. Sequencing data have been deposited in the DDBJ Sequence Read Archive under accession number DRR709131, DRR709132, DRR709133, and DRR709134.

Statistical analysis of scRNA-Seq

Raw FASTQ files were processed and mapped to the mouse reference genome (mm10, GENCODE vM23/Ensembl 98) using the Cell Ranger pipeline (version 4.0, 10x Genomics). Subsequent analyses were performed using R (version 3.6.2) within the RStudio (51) environment (version 1.2.1335). Quality control and primary data processing were conducted using the 'Seurat' package (version 3.2.2) in R (52) (53). Cells expressing fewer than 200 genes were excluded to eliminate low-quality cells. Datasets were merged and normalized using Seurat's SCTransform function. Dimensionality reduction and clustering were performed using RunUMAP, with clustering based on FindNeighbors and FindClusters functions (default parameters). Differentially expressed genes were identified using FindAllMarkers (only.pos = TRUE, min.pct = 0.25, logfc.threshold = 0.25). FindMarkers was used with default parameters for specific pairwise comparisons.

Sertoli cell populations were isolated based on expression of gonadal supporting cell markers (*Gata4*, *Sox9*, *Kitl*, and *Dhh*). Selected cells were visualized using UMAP plots, and clusters expressing markers of other gonadal lineages or high mitochondrial gene content were excluded. Remaining cells were retained for downstream analysis as Sertoli cells.

Germ cells were selected based on *Ddx4* expression and re-visualized on UMAP plots. Clusters expressing somatic markers or showing high mitochondrial gene content were excluded. The remaining cells were analyzed as germ cells. RNA velocity analysis was performed using the Velocyto package (Python 3.7.3) following default settings (54) and visualized using UMAP embeddings generated by Seurat.

Gene enrichment analysis

Gene enrichment analyses were performed using Metascape (55) (v3.5.20250701) with default settings, and results were visualized in Microsoft Excel. To characterize each cluster, we used

the top 100 representative genes per cluster.

Statistics

All experiments were repeated at least three times using biological replicates. Data are presented as mean ± standard deviation (S.D.) or, for box-and-whisker plots, as median, first and third quartiles, and 5th–95th percentiles. Statistical comparisons between groups were primarily performed using the Student's *t*-test. A P value <0.05 was considered statistically significant. *Z*-scores for IP-MS analyses were calculated from Mascot scores. Spearman's correlation coefficients were computed to estimate transcriptional similarity between clusters. P values and adjusted P values (*padj*) during the estimation of Sertoli cell proportions per cluster were calculated using Fisher's exact test. One-way ANOVA was performed to assess statistical significance during the quantification of round spermatids and pachytene spermatocytes.

Data Availability

The LC-MS/MS and scRNA-Seq datasets generated in this study have been deposited in public repositories. Accession numbers are listed in the Materials and Methods section of the main text.

Acknowledgements

We thank Dr. Nishinakamura for generously providing the MYH9 antibody. We are also grateful to members of our laboratory for their insightful discussions and technical support. This work was partially conducted at the Center for Animal Resources and Development and the Research Facilities of the School of Medicine, Kumamoto University.

Author contributions

K.K. designed the study, performed the majority of the experiments, interpreted the data, and wrote the manuscript. T.F. and N.M. contributed to the initial analysis of *Map7* KO mice. K.O. assisted with array tomography analysis. R.S. contributed to scRNA-Seq analysis. S.F. supported histological analysis. K.Y. and S.U. assisted with scRNA-Seq analyses. N.T. conducted the mass spectrometry analysis. A.N. provided advice on IP-MS analysis. K.A. generated the knock-in mice. K.I. provided technical assistance for mouse testis analyses. All authors discussed the results and reviewed the manuscript.

Funding

This study was supported by the Research Program for the Inter-University Research Network for High Depth Omics and the Joint Usage/Research Program for Developmental Medicine, IMEG, Kumamoto University. Additional support was provided by JSPS KAKENHI (Grant Numbers 19K06664, 22K06226, 25K09632, JP16H06280 [ABiS], JP22H04922 [ABiS], and JP16H06276 [AdAMS]); the MEXT Promotion of Development of a Joint Usage/Research System Project: Coalition of Universities for Research Excellence (CURE) Program (Grant Number JPMXP1323015486); and grants from the Narishige Zoological Science Award, the Novartis Foundation for the Promotion of Science, the Mochida Memorial Foundation, the Takeda Science Foundation, and the Uehara Memorial Foundation (to K.K.). Further support was provided by MEXT KAKENHI (JP23H00379, 25H01304), AMED PRIME (21gm6310021h0003), and grants from the Naito Foundation, the Astellas Foundation, and the Takeda Science Foundation (to K.I.).

Conflict of Interest

The authors declare that the research was conducted in the absence of any commercial or financial relationships that could be construed as a potential conflict of interest.

Figure legends

Figure 1. MAP7 exhibits polarized localization to the apical side of microtubule bundles along the apical-basal axis in Sertoli cells.

(**A**) Sections of seminiferous tubules from 8-week-old *Map7-egfp*^{KI} mice were stained for GFP, β-III-tubulin (TUBB3), and DAPI. TUBB3 was used as a Sertoli cell-specific marker. The lower panel shows seminiferous tubules containing step 9–11 spermatids. Scale bar: 50 or 25 μm. (**B**) Sections of seminiferous tubules from 8-week-old *Map7-egfp*^{KI} mice were stained for GFP, acetylated tubulin, and DAPI. The lower panel shows a magnified view of step 9 spermatids. Scale bar: 50, 25, or 10 μm. (**C**) Sections of seminiferous tubules from 8-week-old wild-type mice were stained for MAP7, TUBB3, and DAPI. The lower panel shows seminiferous tubules containing step 9–11 spermatids. Scale bar: 50 or 25 μm.

Figure 2. MAP7 regulates the orientation and morphology of Sertoli cells along the apical-basal axis.

(**A**) Hematoxylin and eosin staining of the sections from testes of the indicated mice (10-, 17-, 21-, 28-, or 35-days old). Biologically independent mice (N = 3) for the indicated genotype were examined. Scale bar: 100 μm. (**B**) The percentage of seminiferous tubules with lumens at the indicated time points was calculated. Data from more than 140 seminiferous tubules from mice (three independent experiments) are indicated and represent the average ± standard deviation (S.D.) (**C**). Array tomography images of seminiferous tubules in mice (10- or 21-day-old). Using a serial-section scanning electron microscope (SEM), 503, 588, 398, or 498 images were obtained at P10 or P21 from *Map7*$^{+/-}$ and *Map7*$^{-/-}$ mice, respectively. Sertoli cells (green), spermatogonia (orange), and spermatocytes (red) were identified based on their nuclear and cellular morphology and adhesion to the basement membrane during the examination of serial-section images. The number represents the ratio of Sertoli cells attached to the basement membrane (upper left, adherent) or Sertoli cell nuclei positioned in the basal layer (lower left, basal nuclei) to the total number of Sertoli cells observed in the stack file (right), providing a visual summary of the quantitative analysis described in the text. The three-dimensional images of Sertoli cells were constructed by manually segmenting serial-section images. Blue or yellow indicates Sertoli cells or basement membrane, respectively. T and L represent views from the transverse and longitudinal axes of the seminiferous tubules, respectively. Scale bar: 10 μm. (**D**) The orientation of Sertoli cell nuclei along the apical–basal axis and actin remodeling on the apical side were analyzed in mice (10- or 17-day-old). To view the orientation of Sertoli cell

nuclei along the apical–basal axis, seminiferous tubules were stained for DAPI and SOX9, allowing detection of Sertoli cell nuclei. Seminiferous tubule morphology was visualized with phalloidin (F-actin) staining. Scale bar: 25 μm. (**E**) The percentage of $SOX9^{+}$ Sertoli cells per cell layer at P10 and P17 was calculated. Data were obtained from more than 145 $SOX9^{+}$ Sertoli cells per mouse (from over ten images collected across three independent experiments) and are presented as mean ± S.D. Statistical comparisons between *Map7*$^{+/-}$ and *Map7*$^{-/-}$ mice were performed for each corresponding layer at P17 using Student's t-test. All three layers showed significant differences between *Map7*$^{+/-}$ and *Map7*$^{-/-}$ mice (*, $P<2.20 \times 10$). (**F**) The germ-independent polarity formation of Sertoli cells was analyzed by eliminating the male germ cell lineage with busulfan treatment. At 28 days old, mice were intraperitoneally injected with busulfan (45 μg/g) and dissected six weeks later for observation using hematoxylin and eosin staining. Biologically independent mice (N = 4) of the specified genotype were examined. Scale bar: 50 μm.

Figure 3. Cytoskeletal remodeling and MAP7 localization during Sertoli cell polarization.

(**A**) Seminiferous tubule sections derived from *Map7-egfp*^{KI} mice (10- or 17-day-old) were stained for GFP, TUBB3, phalloidin (F-actin), and DAPI. Scale bar: 50 μm. (**B**) Confocal imaging of freshly dissected seminiferous tubules from *Map7-egfp*^{KI} mice at P10 (left) and P17 (right). Scale bar: 25 μm.

Figure 4. MAP7 facilitates microtubule remodeling, but not microtubule stabilization, to establish Sertoli cell polarity.

(**A**) The direction and stabilization of microtubule bundles in Sertoli cells were analyzed using three-dimensional projection images from mice (17-day-old). Seminiferous tubule sections were stained with TUBB3 (β-III-tubulin), phalloidin (F-actin), β-catenin, and DAPI. Notably, the proportion of seminiferous tubules in *Map7*$^{-/-}$ mice where TUBB3, F-actin, and β-catenin were abnormally accumulated on the inner side of the tubules was consistent with the proportion of tubules lacking lumen formation, as shown in Fig. 2A, B. Scale bar: 50 or 25 μm. (**B**) High-resolution SEM images were acquired to analyze tight junction formation between Sertoli cells attached to the basement membrane in testes from 10- and 21-day-old mice. The black arrow indicates the Sertoli–Sertoli cell boundary at P10, while the magenta and blue arrows indicate tight junctions and adherens junction–like structures at P21, respectively. The asterisk marks the endoplasmic reticulum. Scale bar: 0.1 μm. (**C**) Tight junction formation of Sertoli cells was analyzed by three-dimensional projection images in the indicated mice (17-days old).

Seminiferous tubules were stained for ZO-1, phalloidin (F-actin), and DAPI. Scale bar: 50 or 25 μm. (**D**) Quantification of the percentage of seminiferous tubules with ectopic ZO-1 was performed based on the images shown in (C). Data are from more than 45 seminiferous tubules in mice (three independent experiments), and represent the average ± S.D. Statistical significance is indicated by $P<0.002$ (Student's *t*-test).

Figure 5. MAP7 coordinates microtubules with actomyosin-associated regulators during Sertoli cell polarization.

(**A**) Immunoprecipitation-mass spectrometry (IP-MS) analysis using *MAP7-egfp*^{KI} HeLa cells. Lysates from wild-type HeLa cells were used as a negative control for immunoprecipitation (IP). Volcano plot of proteins identified in both control and Map7-EGFP^{KI} IP samples, excluding keratin and immunoglobulin-derived proteins. Protein quantification was performed based on Mascot scores. Proteins with a log fold change (Map7-EGFP^{KI} IP / Control IP) > 1 and a z-score > 2 are highlighted in red. Proteins, such as MVP, MAP7, and KIF5B, which had high scores on both metrics, are labeled. (**B**) IP-MS analysis using testes from P17–20 *Map7-egfp*^{KI} mice. Lysates from age-matched wild-type testes were used as the negative control. Volcano plot of proteins identified in both control and MAP7-EGFP^{KI} IP samples, with keratin and immunoglobulin-derived proteins excluded. Proteins with a log fold change > 1 and z-score > 2 are marked in red. Proteins, such as MAP7, MYH9, MYH10, and KIF5B, which had high scores on both metrics, are labeled. (**C**) A Venn diagram comparing interacting proteins identified in *MAP7-egfp*^{KI} HeLa cells and P17–20 *Map7-egfp*^{KI} testes. Ten common interactors were identified, including known MAP7-binding partners, such as KIF5B and its light chain KLC2, as well as TUBB4B, a beta-tubulin isoform. (**D**) Enrichment analysis using Metascape was performed on 22 Sertoli-specific MAP7-interacting proteins identified exclusively in P17–20 *Map7-egfp*^{KI} testes. (**E**) Cytoskeleton-associated proteins that were below the detection limit in the Control-IP are highlighted. Sertoli cell-specific proteins are indicated in red. Proteins are classified based on their association with microtubules (MT), actin filaments (AF), or intermediate filaments (IF). The Mascot score represents a confidence metric generated by the Mascot search engine, indicating the probability that the observed peptide matches correspond to a specific protein in the database. Peptide-spectrum match (PSM) denotes the number of spectra that confidently match a given peptide, reflecting the reliability of peptide identification. (**F**) Testes from 17-day-old *Map7*$^{+/-}$ mice were subjected to immunofluorescence analysis. Cross-sections of seminiferous tubules were stained with antibodies against TUBB3, MYH9, and phalloidin for F-actin, along with DAPI for nuclear visualization. Scale bar: 25 μm. (**G**)

Higher-magnification imaging of MYH9 localization in Sertoli cells. Testes from 17-day-old *Map7*$^{+/-}$ and *Map7*$^{-/-}$ mice were analyzed by immunofluorescence. Cross-sections of seminiferous tubules were stained with antibodies against TUBB3 and MYH9, and with phalloidin to visualize F-actin, together with DAPI to label nuclei. For better visibility, only the grayscale channels of TUBB3, MYH9, and phalloidin for F-actin are shown. Lower-magnification images corresponding to these fields are presented in Supplemental Fig. 5. Scale bar: 10 μm.

Figure 6. Functional differentiation of Sertoli cells is largely preserved in the absence of MAP7.

(**A**) UMAP visualization of transcriptomic profiles from Sertoli cells isolated from P19 testes of the indicated genotypes. The control sample was prepared by pooling testes from one wild-type and two *Map7*$^{+/-}$ littermate mice; testes from *Map7*$^{-/-}$ littermates were used for comparison. Clusters were defined based on distinct gene expression patterns. (**B**) Violin plots showing the expression of cluster-specific gene sets, selected from the top 100 differentially expressed genes in each cluster, as identified by Metascape enrichment analysis. (**C**) Control and *Map7*$^{-/-}$ Sertoli cells were visualized separately using UMAPs constructed in Seurat. Using the same datasets, pseudotime trajectories were inferred with Monocle3. For root selection, shared_score (cluster overlap), specificity_score (cluster uniqueness), and entropy_score (transcriptional diversity) were computed, resulting in cluster 1 being selected as the root. The numbers of nodes, edges, branch points, average degree, and diameter of each trajectory are shown below the corresponding UMAPs. (**D**) Distribution of normalized pseudotime values (0–1) across clusters for control and *Map7*$^{-/-}$ Sertoli cells. Violin plots with embedded boxplots highlight relative shifts in pseudotime positioning between genotypes. (**E**) Proportions of Sertoli cells assigned to each cluster in control and Map7–/– testes. Statistical differences were assessed using Fisher's exact test; *P* values and adjusted *P* values (*padj*) are shown.

Figure 7. Sertoli apical domain ensures orderly progression of the pachytene stage during meiosis.

(**A**) Whole-mount immunofluorescence of seminiferous tubules from 8-week-old mice showing GFRα1^{+} spermatogonial stem cells (SSCs). Tubules were stained for GFRα1 and DAPI and imaged from the basal side by z-sectioning. Scale bar, 50 μm. (**B**) Quantification of GFRα1^{+} SSCs per 10^4 μm^2 based on the basal area of seminiferous tubules. Data were collected from 40 tubules per genotype across three independent experiments. (**C**) Immunofluorescence

analysis of ZFP541^{+} round spermatids and SYCP3^{+}/ZFP541^{+} pachytene spermatocytes in testis sections from 8-week-old mice. Sections were stained with PNA (acrosome marker), SYCP3, ZFP541, and DAPI. Scale bars, 50 and 25 μm. (**D**) Quantification of ZFP541^{+} round spermatids (RS) and SYCP3^{+}/ZFP541^{+} pachytene spermatocytes (Pachy Sp) per 10^{3} μm^{2}. Data were obtained from 28 images per genotype across three independent experiments. Statistical significance was assessed by one-way ANOVA (P<0.003), followed by the Student's t-test, with significance indicated as follows: *, $P<4\times10^{-6}$; **, $P<4\times10^{-5}$. (**E**) UMAP visualization of scRNA-Seq transcriptomic profiles from germ cells isolated from 23-day-old testes from specified genotypes. Clusters were defined based on gene expression patterns. Arrows indicate the direction of germ cell differentiation. Spg, Sp, and RS denote spermatogonia, spermatocytes, and round spermatids, respectively. (**F**) Proportions of indicated germ cell types within each cluster in the indicated mice. To further resolve spermatocyte sub-stages, expression levels of sex chromosomal genes (bottom panel) were assessed and visualized as violin plots to assist in stage classification. (**G**) Clustered UMAP representations of specified genotypes (left panel). *Prelid1*, a gene expressed through early pachytene (middle panel), and *Ccna1*, a late pachytene-enriched gene (right panel), were used as molecular markers to classify clusters f–j into early, mid, or late pachytene stages.

References

1. L. O'Donnell, L. B. Smith, D. Rebourcet, Sertoli cells as key drivers of testis function. *Seminars in cell & developmental biology* **121**, 2-9 (2022).
2. P. S. Tanwar, T. Kaneko-Tarui, L. Zhang, J. M. Teixeira, Altered LKB1/AMPK/TSC1/TSC2/mTOR signaling causes disruption of Sertoli cell polarity and spermatogenesis. *Human Molecular Genetics* **21**, 4394-4405 (2012).
3. Z. Xiong *et al.*, Raptor directs Sertoli cell cytoskeletal organization and polarity in the mouse testis†. *Biology of Reproduction* **99**, 1289-1302 (2018).
4. A. Heinrich, B. Bhandary, S. J. Potter, N. Ratner, T. DeFalco, Cdc42 activity in Sertoli cells is essential for maintenance of spermatogenesis. *Cell reports* **37**, 109885 (2021).
5. A. Heinrich, S. J. Potter, L. Guo, N. Ratner, T. DeFalco, Distinct Roles for Rac1 in Sertoli Cell Function during Testicular Development and Spermatogenesis. *Cell reports* **31**, 107513 (2020).
6. J. E. M. Dunleavy, M. K. O'Bryan, P. G. Stanton, L. O'Donnell, The cytoskeleton in spermatogenesis. *Reproduction (Cambridge, England)* **157**, R53-R72 (2019).
7. B. D. Grove, A. W. Vogl, Sertoli cell ectoplasmic specializations: a type of actin-associated adhesion junction? *Journal of Cell Science* **93**, 309-323 (1989).
8. S. Byers, R. Graham, H. N. Dai, B. Hoxter, Development of Sertoli cell junctional specializations and the distribution of the tight-junction-associated protein ZO-1 in the mouse testis. *American Journal of Anatomy* **191**, 35-47 (1991).
9. S. L. Fleming, P. R. Shank, K. Boekelheide, γ-Tubulin Overexpression in Sertoli Cells In Vivo: I. Localization to Sites of Spermatid Head Attachment and Alterations in Sertoli Cell Microtubule Distribution1. *Biology of Reproduction* **69**, 310-321 (2003).
10. S. L. Fleming, P. R. Shank, K. Boekelheide, γ-Tubulin Overexpression in Sertoli Cells In Vivo. II: Retention of Spermatids, Residual Bodies, and Germ Cell Apoptosis1. *Biology of Reproduction* **69**, 322-330 (2003).
11. F. Wang, Q. Zhang, J. Cao, Q. Huang, X. Zhu, The microtubule plus end-binding protein EB1 is involved in Sertoli cell plasticity in testicular seminiferous tubules. *Experimental Cell Research* **314**, 213-226 (2008).
12. L. B. Smith *et al.*, KATNAL1 Regulation of Sertoli Cell Microtubule Dynamics Is Essential for Spermiogenesis and Male Fertility. *PLOS Genetics* **8**, e1002697 (2012).
13. A. Roll-Mecak, The Tubulin Code in Microtubule Dynamics and Information Encoding. *Dev. Cell* **54**, 7-20. (2020).
14. J. M. Cleary, W. O. Hancock, Molecular mechanisms underlying microtubule growth

dynamics. *Curr. Biol.* **31**, R560-R573. (2021).

15. K. Barlan, W. Lu, V. I. Gelfand, The microtubule-binding protein ensconsin is an essential cofactor of kinesin-1. *Curr. Biol.* **23**, 317-322. (2013).

16. T. Metzger *et al.*, MAP and kinesin-dependent nuclear positioning is required for skeletal muscle function. *Nature* **484**, 120-124 (2012).

17. H. H. Sung *et al.*, Drosophila ensconsin promotes productive recruitment of Kinesin-1 to microtubules. *Dev. Cell* **15**, 866-876. (2008).

18. K. Kikuchi *et al.*, Map7/7D1 and Dvl form a feedback loop that facilitates microtubule remodeling and Wnt5a signaling. *EMBO Rep.* **19**, e45471. (2018).

19. S. R. Tymanskyj, B. H. Yang, K. J. Verhey, L. Ma, MAP7 regulates axon morphogenesis by recruiting kinesin-1 to microtubules and modulating organelle transport. *Elife* **7**, e36374. (2018).

20. P. J. Hooikaas *et al.*, MAP7 family proteins regulate kinesin-1 recruitment and activation. *J. Cell Biol.* **218**, 1298-1318. (2019).

21. K. Kikuchi *et al.*, Map7D2 and Map7D1 facilitate microtubule stabilization through distinct mechanisms in neuronal cells. *Life science alliance* **5** (2022).

22. X. Pan *et al.*, MAP7D2 Localizes to the Proximal Axon and Locally Promotes Kinesin-1-Mediated Cargo Transport into the Axon. *Cell Rep.* **26**, 1988-1999. (2019).

23. A. Adler *et al.*, A structural and dynamic visualization of the interaction between MAP7 and microtubules. *Nat Commun* **15**, 1948 (2024).

24. B. Y. Monroy *et al.*, Competition between microtubule-associated proteins directs motor transport. *Nat. Commun.* **9**, 1487. (2018).

25. B. Y. Monroy *et al.*, A Combinatorial MAP Code Dictates Polarized Microtubule Transport. *Dev. Cell* **53**, 60-72.e64. (2020).

26. N. Fabre-Jonca *et al.*, The distribution of murine 115-kDa epithelial microtubule-associated protein (E-MAP-115) during embryogenesis and in adult organs suggests a role in epithelial polarization and differentiation. *Differentiation; research in biological diversity* **63**, 169-180 (1998).

27. M. Komada, D. J. McLean, M. D. Griswold, L. D. Russell, P. Soriano, E-MAP-115, encoding a microtubule-associated protein, is a retinoic acid-inducible gene required for spermatogenesis. *Genes Dev* **14**, 1332-1342 (2000).

28. L. D. Russell, A. Bartke, J. C. Goh, Postnatal development of the Sertoli cell barrier, tubular lumen, and cytoskeleton of Sertoli and myoid cells in the rat, and their relationship to tubular fluid secretion and flow. *The American journal of anatomy* **184**,

179-189 (1989).

29. A. Willems *et al.*, Selective ablation of the androgen receptor in mouse sertoli cells affects sertoli cell maturation, barrier formation and cytoskeletal development. *PLoS One* **5**, e14168 (2010).

30. A. Bashamboo *et al.*, Human Male Infertility Associated with Mutations in NR5A1 Encoding Steroidogenic Factor 1. *The American Journal of Human Genetics* **87**, 505-512 (2010).

31. A. Ferlin *et al.*, Male infertility and androgen receptor gene mutations: clinical features and identification of seven novel mutations. *Clinical Endocrinology* **65**, 606-610 (2006).

32. J. G. Flanagan, D. C. Chan, P. Leder, Transmembrane form of the kit ligand growth factor is determined by alternative splicing and is missing in the SId mutant. *Cell* **64**, 1025-1035 (1991).

33. O. Hiort *et al.*, Significance of mutations in the androgen receptor gene in males with idiopathic infertility. *The Journal of clinical endocrinology and metabolism* **85**, 2810-2815 (2000).

34. C. K. Naughton, S. Jain, A. M. Strickland, A. Gupta, J. Milbrandt, Glial Cell-Line Derived Neurotrophic Factor-Mediated RET Signaling Regulates Spermatogonial Stem Cell Fate1. *Biology of Reproduction* **74**, 314-321 (2006).

35. J. P. Luaces, N. Toro-Urrego, M. Otero-Losada, F. Capani, What do we know about blood-testis barrier? current understanding of its structure and physiology. *Front Cell Dev Biol* **11**, 1114769 (2023).

36. M. C. Hofmann, E. McBeath, Sertoli Cell-Germ Cell Interactions Within the Niche: Paracrine and Juxtacrine Molecular Communications. *Front Endocrinol (Lausanne)* **13**, 897062 (2022).

37. M. J. Oatley, K. E. Racicot, J. M. Oatley, Sertoli cells dictate spermatogonial stem cell niches in the mouse testis. *Biol Reprod* **84**, 639-645 (2011).

38. K. I. Ishiguro *et al.*, MEIOSIN Directs the Switch from Mitosis to Meiosis in Mammalian Germ Cells. *Dev Cell* **52**, 429-445.e410 (2020).

39. T. Watanabe, E. C. Cheng, M. Zhong, H. Lin, Retrotransposons and pseudogenes regulate mRNAs and lncRNAs via the piRNA pathway in the germline. *Genome Res* **25**, 368-380 (2015).

40. C. Sweeney *et al.*, A distinct cyclin A is expressed in germ cells in the mouse. *Development* **122**, 53-64 (1996).

41. F. Haque *et al.*, Non-muscle myosin II deletion in the developing kidney causes ureter-bladder misconnection and apical extrusion of the nephric duct lineage epithelia. *Developmental Biology* **427**, 121-130 (2017).
42. W. Du *et al.*, Myosin II mediates Shh signals to shape dental epithelia via control of cell adhesion and movement. *PLoS Genet* **20**, e1011326 (2024).
43. L. Nel-Themaat *et al.*, Morphometric analysis of testis cord formation in Sox9-EGFP mice. *Dev Dyn* **238**, 1100-1110 (2009).
44. T. Sakuma, S. Nakade, Y. Sakane, K. T. Suzuki, T. Yamamoto, MMEJ-assisted gene knock-in using TALENs and CRISPR-Cas9 with the PITCh systems. *Nature protocols* **11**, 118-133 (2016).
45. J. Schindelin *et al.*, Fiji: an open-source platform for biological-image analysis. *Nat Methods* **9**, 676-682 (2012).
46. R. C. Team, R: A Language and Environment for Statistical Computing. *R Foundation for Statistical Computing, Vienna, Austria* (2021).
47. I. Takagi *et al.*, Penetration and Stainability of Modified Sato's Lead Staining Solution. *Journal of Electron Microscopy* **39**, 67-68 (1990).
48. I. Belevich, M. Joensuu, D. Kumar, H. Vihinen, E. Jokitalo, Microscopy Image Browser: A Platform for Segmentation and Analysis of Multidimensional Datasets. *PLoS Biol* **14**, e1002340 (2016).
49. A. Bairoch, R. Apweiler, The SWISS-PROT protein sequence data bank and its supplement TrEMBL in 1999. *Nucleic Acids Res* **27**, 49-54 (1999).
50. S. Okuda *et al.*, jPOST environment accelerates the reuse and reanalysis of public proteome mass spectrometry data. *Nucleic Acids Research* **53**, D462-D467 (2024).
51. P. team, RStudio: Integrated Development Environment for R. *Posit Software, PBC, Boston, MA, USA* (2025).
52. A. Butler, P. Hoffman, P. Smibert, E. Papalexi, R. Satija, Integrating single-cell transcriptomic data across different conditions, technologies, and species. *Nat Biotechnol* **36**, 411-420 (2018).
53. T. Stuart *et al.*, Comprehensive Integration of Single-Cell Data. *Cell* **177**, 1888-1902 e1821 (2019).
54. G. La Manno *et al.*, RNA velocity of single cells. *Nature* **560**, 494-498 (2018).
55. Y. Zhou *et al.*, Metascape provides a biologist-oriented resource for the analysis of systems-level datasets. *Nat Commun* **10**, 1523 (2019).

Kikuchi_Figure 1

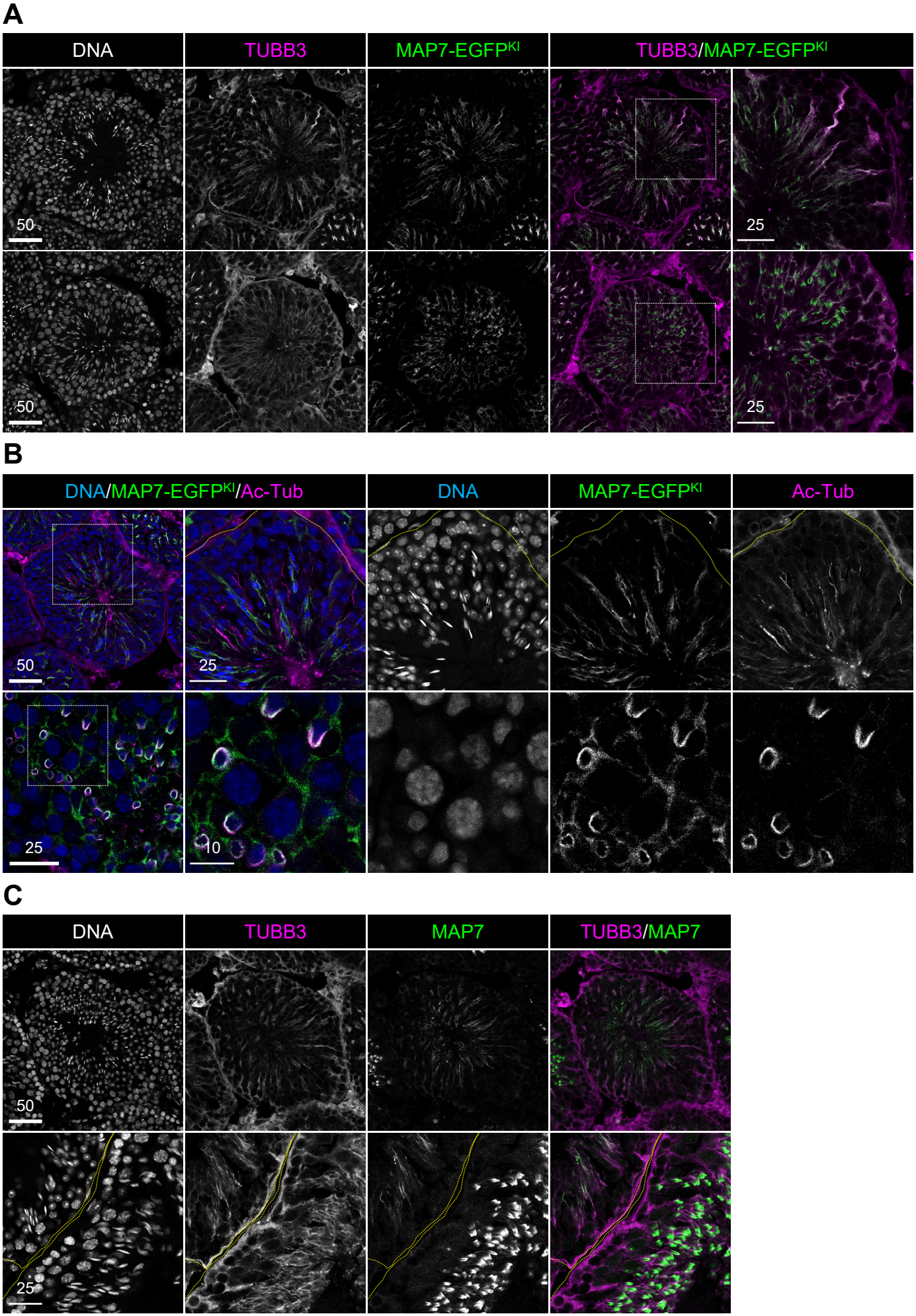

Kikuchi_Figure 2

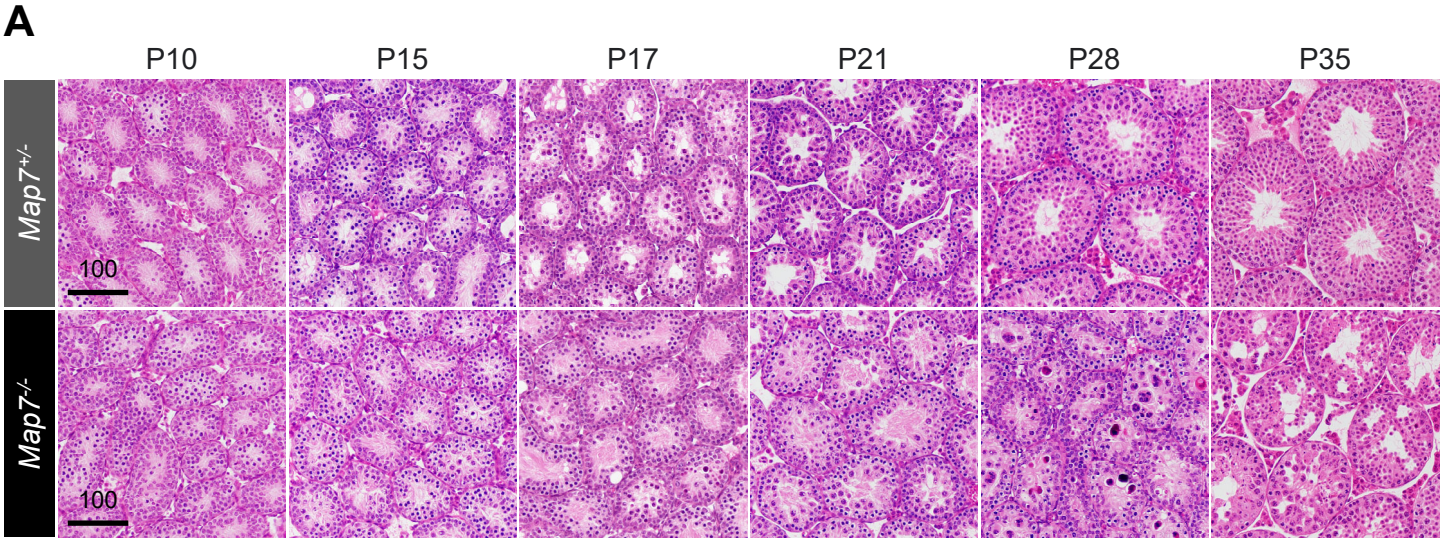

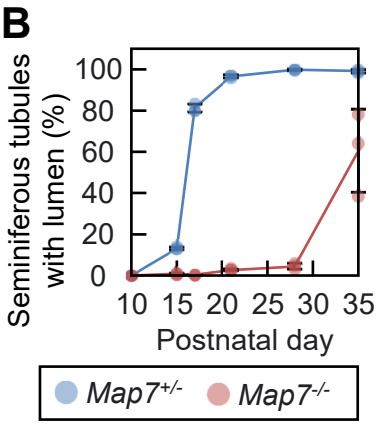

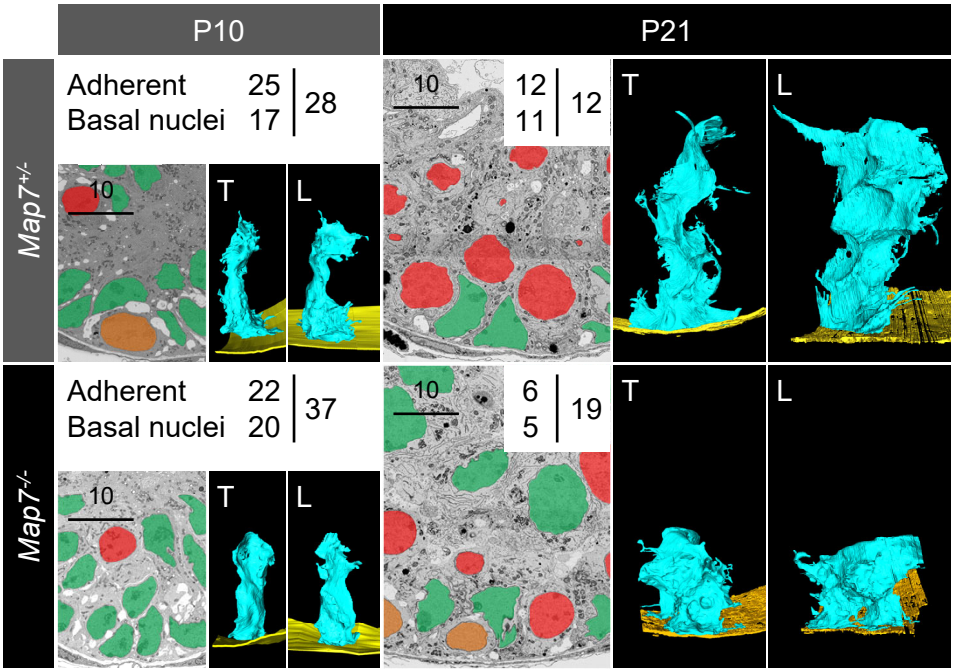

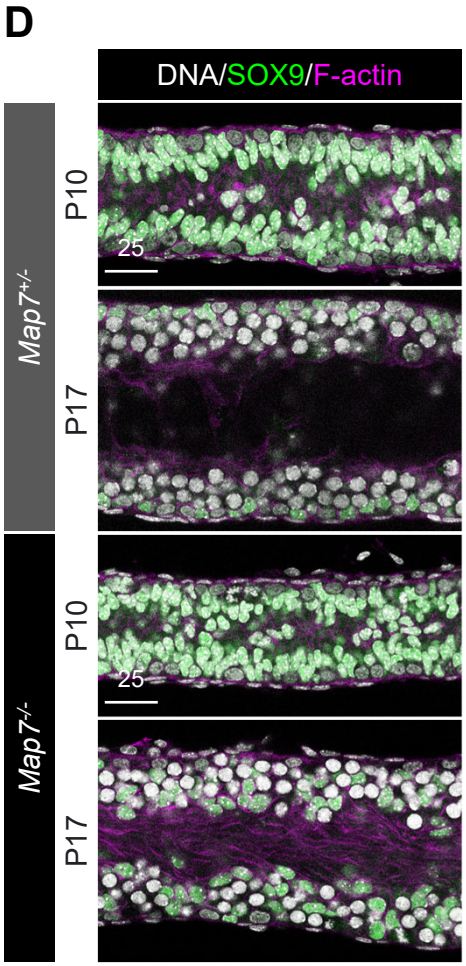

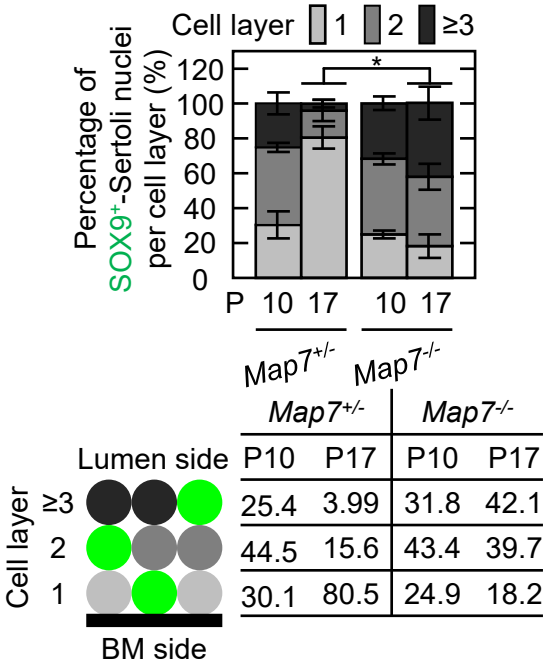

	Map7+/-		Map7-/-	
	P10	P17	P10	P17
≥3	25.4	3.99	31.8	42.1
2	44.5	15.6	43.4	39.7
1	30.1	80.5	24.9	18.2

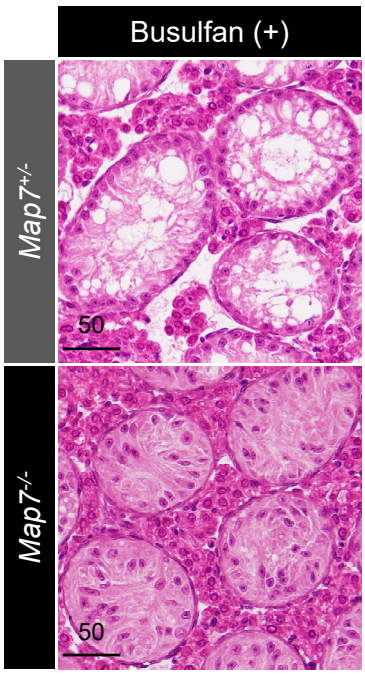

Kikuchi_Figure 3

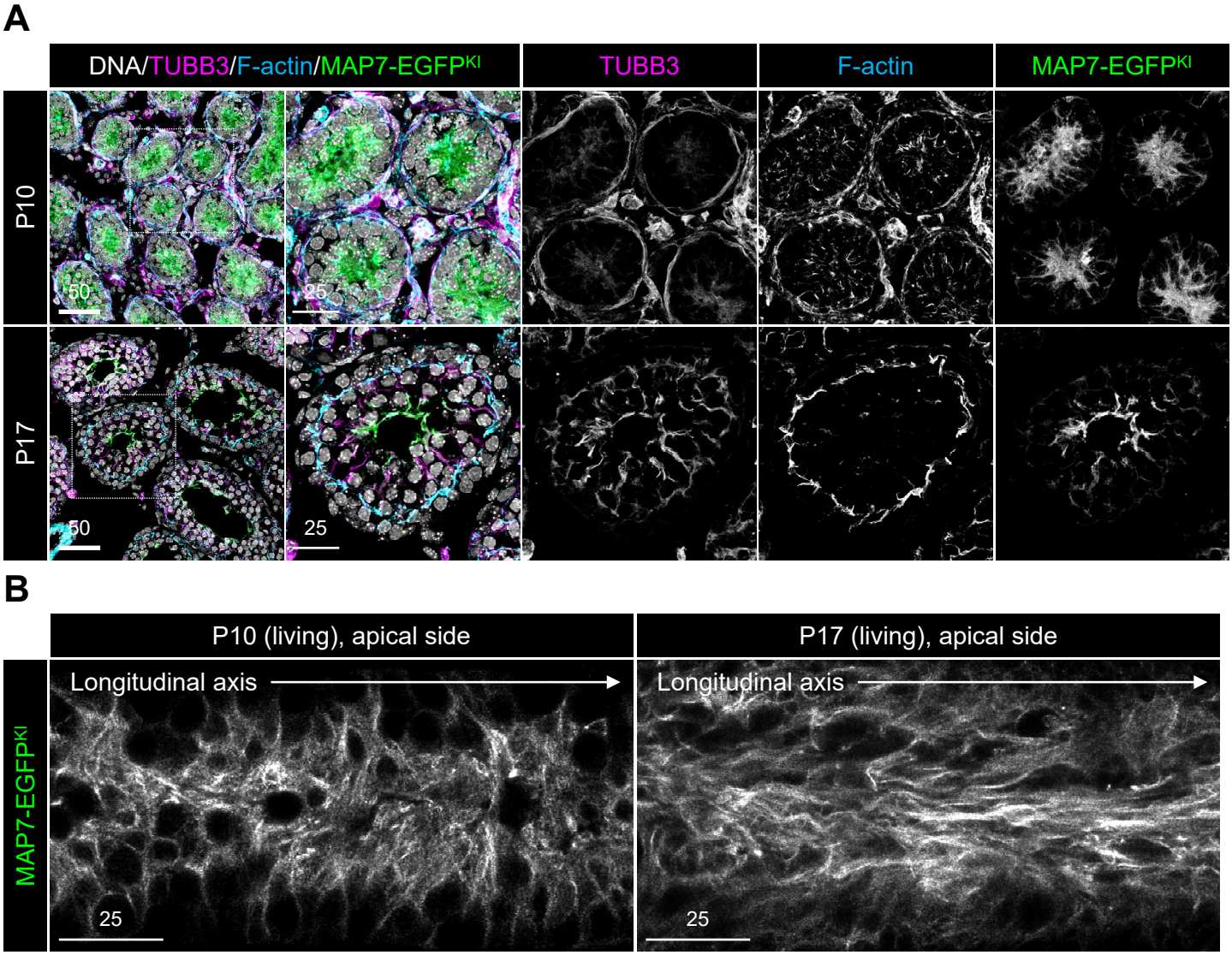

Kikuchi_Figure 4

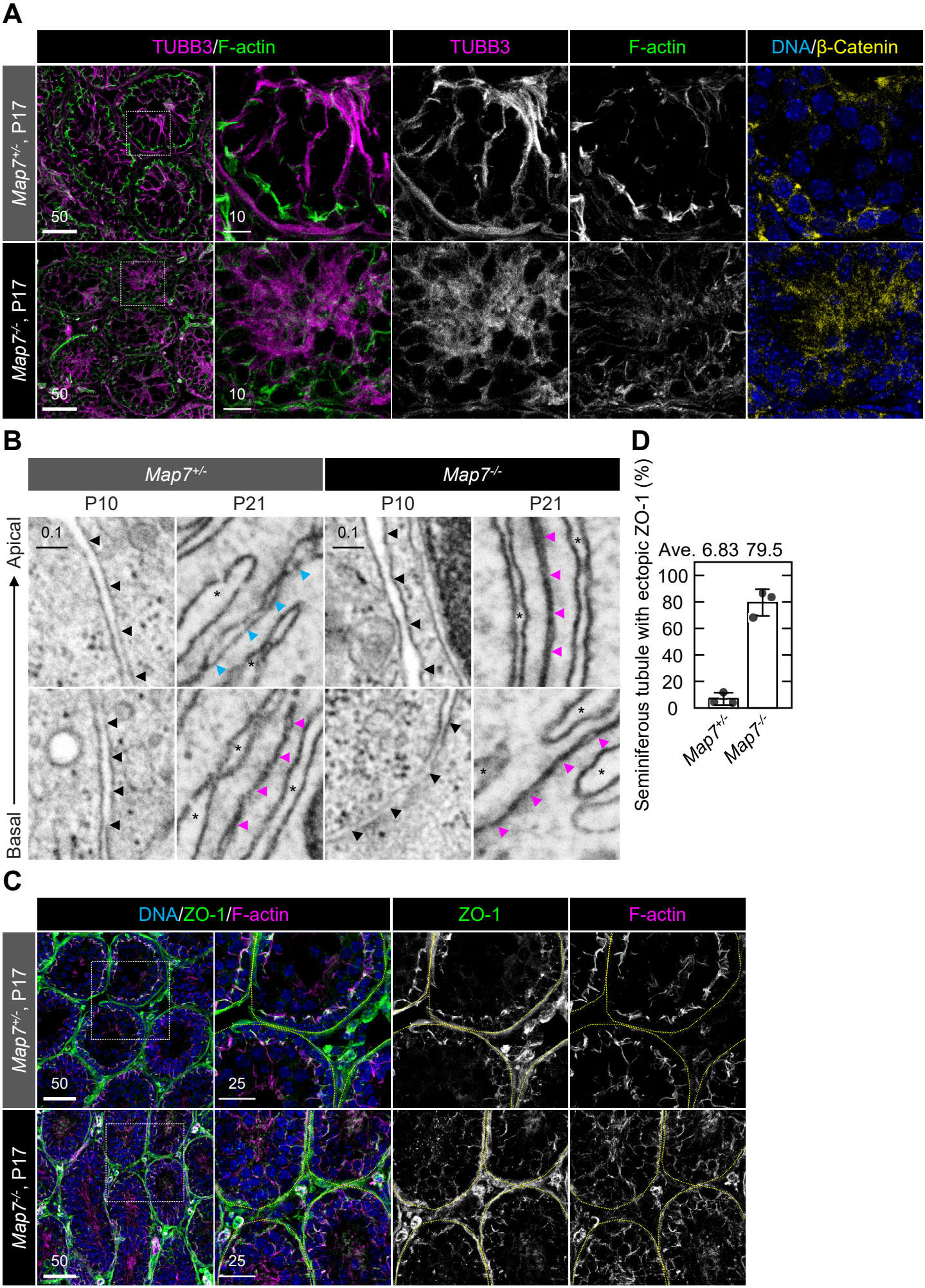

Kikuchi_Figure 5

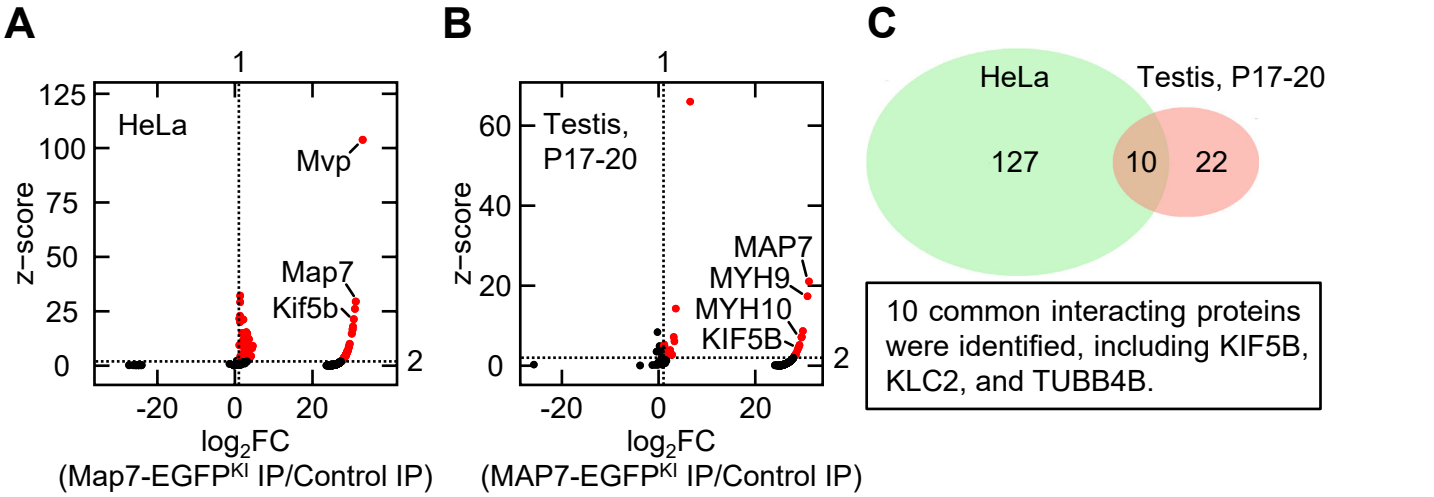

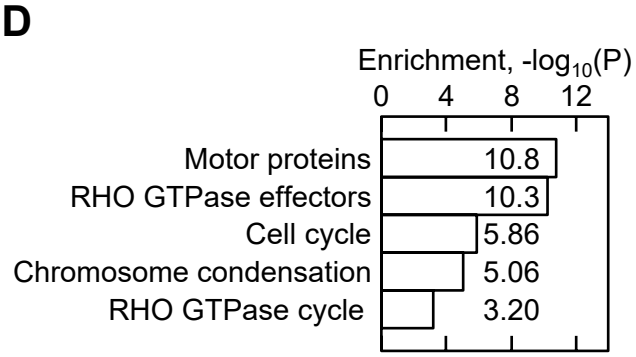

E

	Name	log_2FC	z-score	Mascot score	PSMs
MT	MAP7	31.08339	21.07687	2275.273	172
MT	KIF5B	28.90763	4.437005	503.575	24
MT	TUBB3	28.41413	3.06684	357.6893	18
MT	KLC2	28.0491	2.315854	277.7294	16
AF	MYH9	30.8082	17.36587	1880.151	90
AF	ACTC1	29.83043	8.673716	954.6707	43
AF	MYH10	29.5447	7.062721	783.1432	44
IF	VIM	28.92826	4.505102	510.8255	24

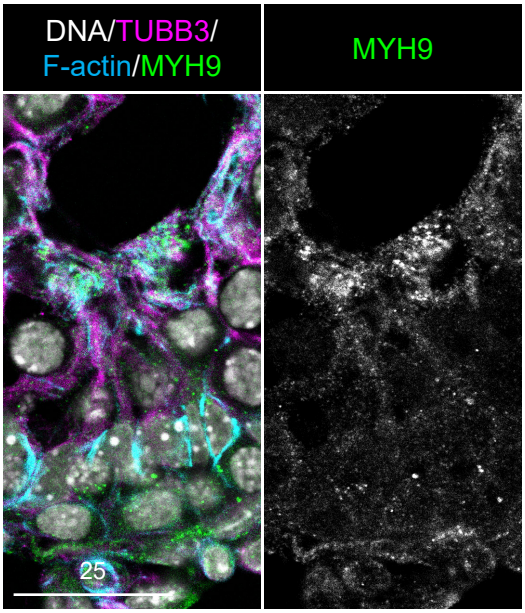

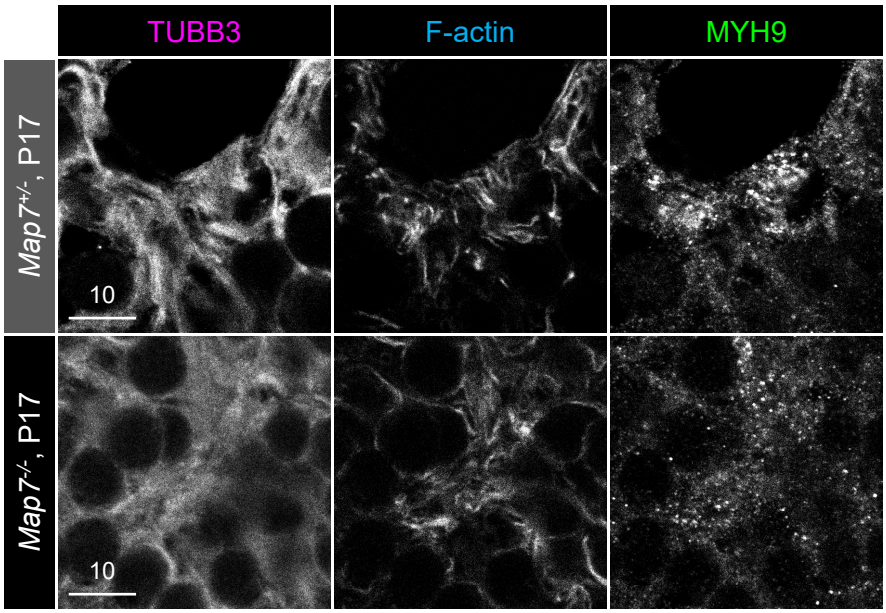

Kikuchi_Figure 6

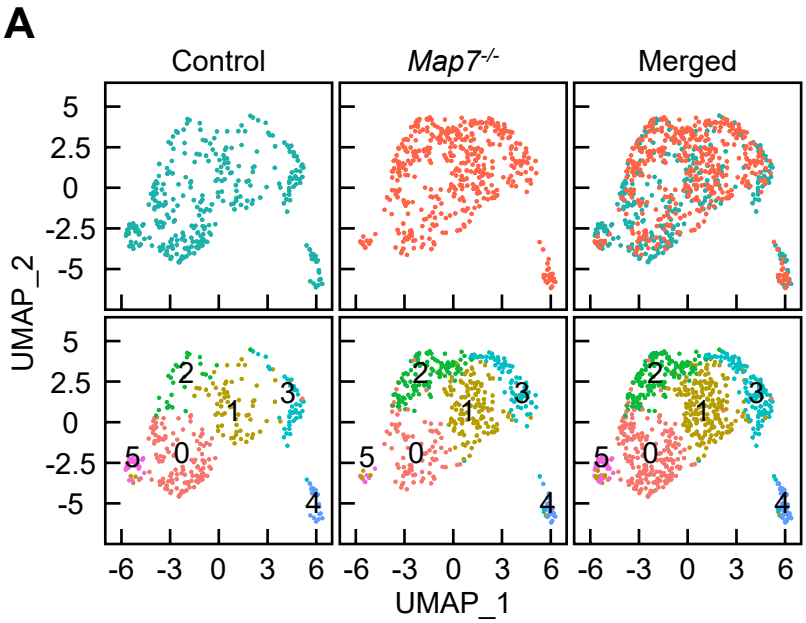

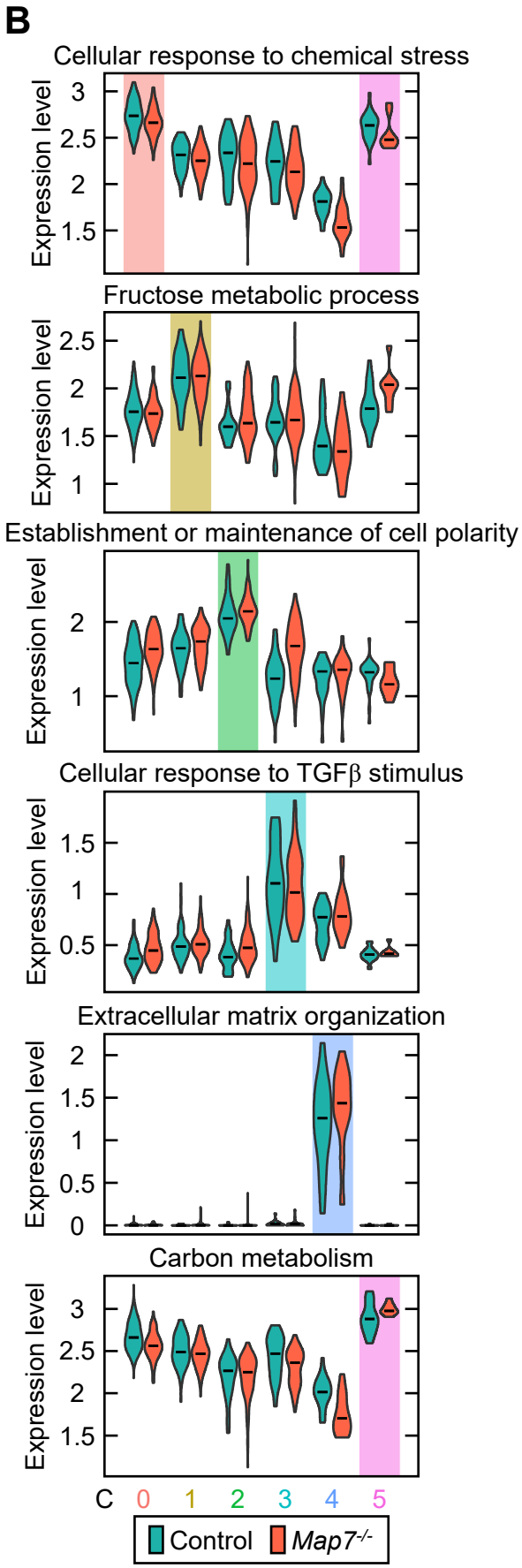

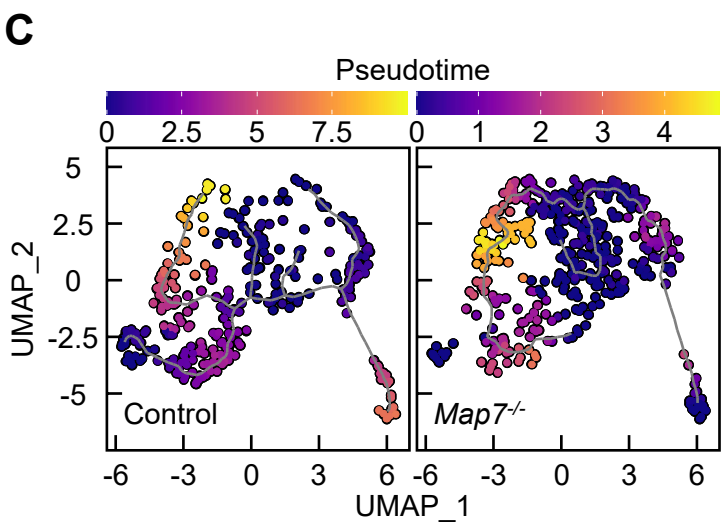

	Nodes	Edges	Branch points	Avg. degree	Diameter
Control	148	147	4	1.99	74
Map7$^{-/-}$	131	130	1	1.98	102

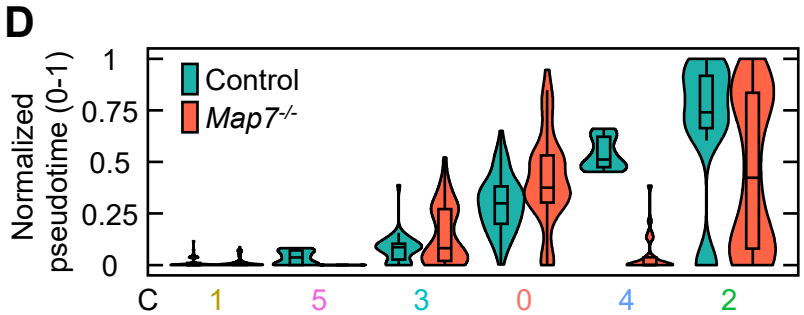

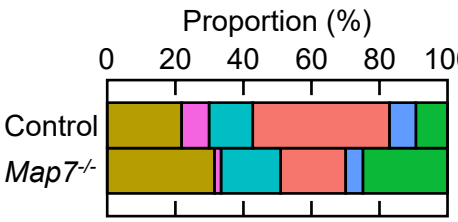

C	*P* value	*padj*
1	3.60e-03	5.40e-03
5	8.37e-05	1.67e-04
3	1.01e-01	1.21e-01
0	3.83e-10	2.30e-09
4	1.65e-01	1.65e-01
2	3.24e-08	9.71e-08
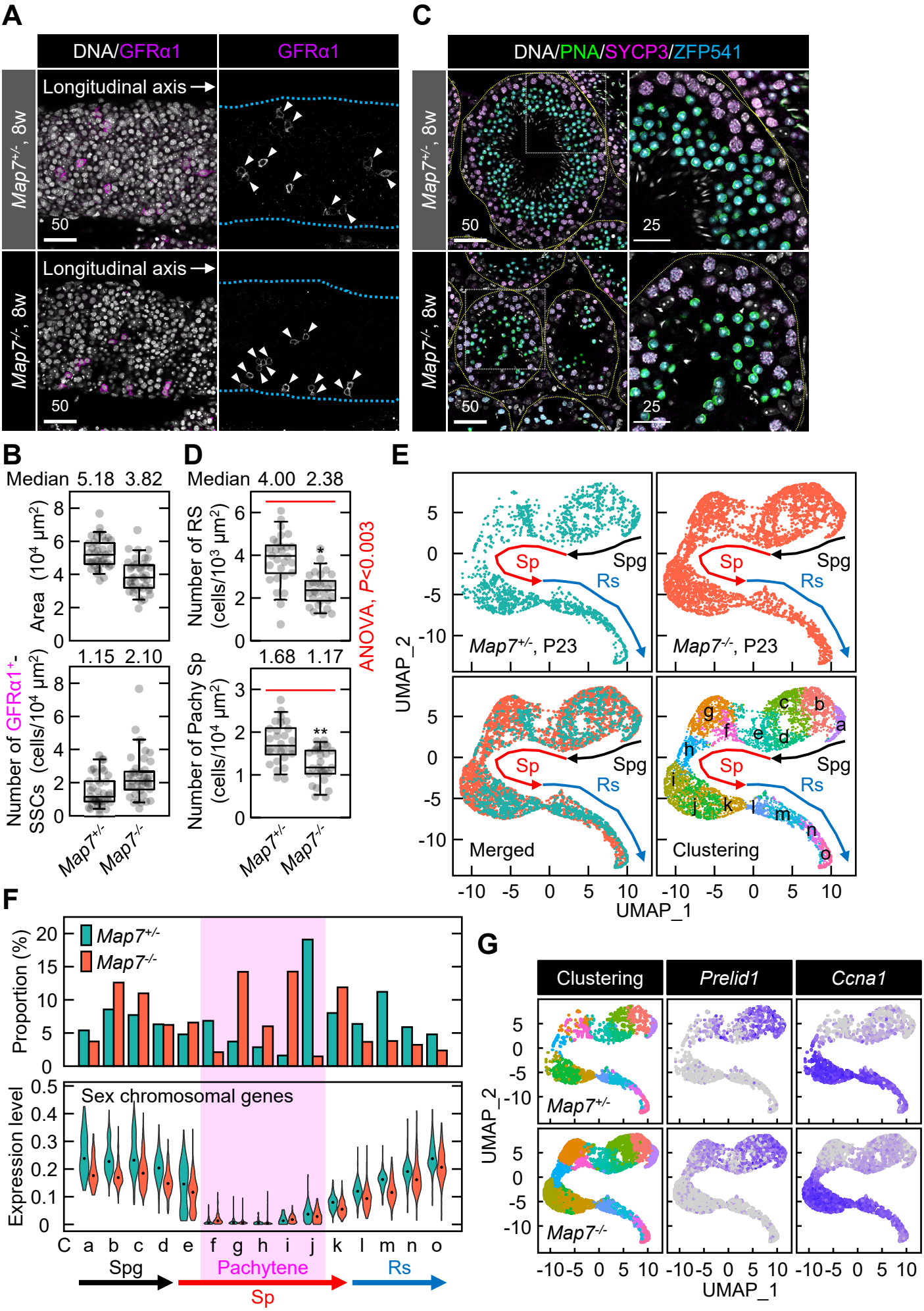
Kikuchi_Figure 7